

Review

A Review of Skin-Wearable Sensors for Non-Invasive Health Monitoring Applications

Pengsu Mao ^{1,2}, Haoran Li ^{1,2} and Zhibin Yu ^{1,2,*}

¹ Department of Industrial and Manufacturing Engineering, FAMU-FSU College of Engineering, Florida State University, Tallahassee, FL 32310, USA

² High-Performance Materials Institute, Florida State University, Tallahassee, FL 32310, USA

* Correspondence: zyu@fsu.edu

Abstract: The early detection of fatal diseases is crucial for medical diagnostics and treatment, both of which benefit the individual and society. Portable devices, such as thermometers and blood pressure monitors, and large instruments, such as computed tomography (CT) and X-ray scanners, have already been implemented to collect health-related information. However, collecting health information using conventional medical equipment at home or in a hospital can be inefficient and can potentially affect the timeliness of treatment. Therefore, on-time vital signal collection via healthcare monitoring has received increasing attention. As the largest organ of the human body, skin delivers significant signals reflecting our health condition; thus, receiving vital signals directly from the skin offers the opportunity for accessible and versatile non-invasive monitoring. In particular, emerging flexible and stretchable electronics demonstrate the capability of skin-like devices for on-time and continuous long-term health monitoring. Compared to traditional electronic devices, this type of device has better mechanical properties, such as skin conformal attachment, and maintains compatible detectability. This review divides the health information that can be obtained from skin using the sensor aspect's input energy forms into five categories: thermoelectrical signals, neural electrical signals, photoelectrical signals, electrochemical signals, and mechanical pressure signals. We then summarize current skin-wearable health monitoring devices and provide outlooks on future development.



Citation: Mao, P.; Li, H.; Yu, Z. A Review of Skin-Wearable Sensors for Non-Invasive Health Monitoring Applications. *Sensors* **2023**, *23*, 3673. <https://doi.org/10.3390/s23073673>

Academic Editors: Chao Liu, Wenfeng Zheng, Mingzhe Liu, Dan Wang and Kenan Li

Received: 28 February 2023
Revised: 24 March 2023
Accepted: 27 March 2023
Published: 31 March 2023



Copyright: © 2023 by the authors. Licensee MDPI, Basel, Switzerland. This article is an open access article distributed under the terms and conditions of the Creative Commons Attribution (CC BY) license (<https://creativecommons.org/licenses/by/4.0/>).

Keywords: wearable sensors; health monitoring; non-invasive; stretchable; big data

1. Introduction

Health-related issues are among the most vital topics affecting the continuation of humanity. Since the last century, modern medical systems and techniques have developed rapidly, prolonging lives by fighting against illness. While routine physical checkups and post-morbid consultations are two major approaches used to track many health problems, the danger of sudden illness still threatens our lives. Therefore, opportune medical diagnosis and treatment have gradually taken center stage. On-time continuous health monitoring offers us an opportunity to identify diseases in an early stage and minimize risks. Although it is easy to implement continuous monitoring in hospitals, limited medical resources and expensive medical expenses are prohibitive, especially for areas with unequal resources. To detect diseases in an early stage and provide greater accessibility to the public, one of the success solution paths is focusing on non-invasive health monitoring for on-time detection, data collection, and initial diagnosis. Our skin, which works as the interface between the deep tissues and the external environment, is an effective and suitable medium for non-invasive health monitoring, since it can reflect important signals related to our health status. Due to the accessibility of skin and the natural sensors we are equipped with, the earliest record of exploring physiological signals from skin can be tracked back to 400 BC, when people first detected that body temperature can be an index of illness [1]. The

natural sensors of our body allow us to perceive temperature, pressure, taste, odor, light, etc. Advances in solid-state electronics over the last century have expanded horizons in sensing, leading to today's sensors outputting electrical signals that are collected and processed almost entirely by computers. Such technology has been clinically utilized for health monitoring and has been continuously improved in terms of high sensitivity and safety; however, most applications are limited to clinics due to being bulky [2], expensive [3], and immobile [4], and requiring easy-drying electrolyte gels [5,6], all of which ultimately lead to difficulties in long-term monitoring [7]. In addition, the electronic components need to be attached to the skin due to inflexible rigid contact [8–12]. The vulnerable, non-conformal adhesive design leads to low measurement sensitivity and significant measurement error, especially during movement [13]. To overcome these limitations, a new generation of skin-wearable devices has emerged. This review includes studies and learnings on flexible and stretchable non-invasive skin-wearable electronics and classifies them according to their input energy form, i.e., thermoelectrical signals, neural electrical signals, photoelectrical signals, mechanical signals, and electrochemical signals.

2. Systematic Review of Skin-Wearable Health Monitoring Strategies

The epidermis and dermis bilayer of skin can be treated as a three-dimensional network of collagen fibers that straighten during stretching parallel to the applied load direction [14,15]. This property results in a high dependence between human skin and applied force orientation. The stretchability of the skin depends on whether the fibers are oriented. The fibers that cross Langer's lines are less stretchable than fibers that are parallel to the lines [16]. The elastic deform strain of the skin can range from 20 to 30% with elastic modules ranging from 1.11 kpa to 57 Mpa depending on age, skin location, and testing methods [17–24]. Such behavior can be treated as the soft substrate for skin-wearable devices, and similar mechanical properties across electronic devices are required to achieve conformal contact with skin and to help patients tolerate the deformation during normal body stretching.

In addition to the substrates, the mechanical properties of sensing elements are also significant. This problem can be solved by three approaches: material selection, substrate pre-strain, and device structure. Solution-processed electronics and dispersible conducting/semiconducting nanomaterials are applied in the two major approaches to enhance electronic flexibility from a material aspect. The solution-processed sensors can be deposited onto the large-area soft substrates that are solvent-compatible with the material [25]. The manufacturing techniques, including spin coating, inkjet printing, spray coating, and doctor blade printing, are particularly useful for organic materials such as thermoelectric and optoelectronic materials [25–27]. However, the flexibility/stretchability of the devices is limited by both substrate and sensing elements. The stretchability can be greatly enhanced by embedding dispersible conducting/semiconducting nanomaterials, including nanoparticles [5], nanowires [28], nanotubes [29,30], and graphene into an elastomer matrix [30]. The preferred growth direction of the nanowires is difficult to control due to the spontaneous network formation of the 3D structure [31]. In addition, elastomeric materials have been used to embed/support rigid sensing components to achieve device stretchability. In the recent study, a bioadhesive hydrogel elastomer couplant was used as the stretchable substrate for rigid ultrasound probss [32]. The device can be attached to plenty of locations on our body for 48 h to continuously monitor acoustic signals from blood flow, the lungs, and the heart. The second approach is to apply a pre-strain to the stretchable substrate that uses buckles perpendicular to the axis, which impart elastic properties to the non-stretchable organic electronics [33]. The result shows that when applying 80% pre-strain on the stretchable substrate before applying the solution-processed organic electronics, the organic electronic device is able to maintain the electric property with restretching strain <80% [34]. Although this approach provides stretchability to non-stretchable organic electronics, the device cannot be stretched beyond the value and direction of pre-strain. Additionally, the devices cannot return to their original length after fabrication and release

of pre-strain. The third strategy is using the filamentary serpentine (FS) or fractal geometry for sensing elements and electrodes [31]. The FS exploits the high-order iterative self-similar fractal patterns to design the conductive traces with strain orientations. This kind of curve can fill any arbitrary shape in a small area, maximize skin-electronic contact area, and effectively reduce the impedance. The sensing part is generally made by sandwiching ultrathin gold/chromium (Cr/Au) traces between polyimide(PI) layers due to their high resistance to atmospheric corrosion, the low resistivity of the Cr/Au combination, and the adhesion improvement of Cr [35]. The fractal traces can be further mounted on skin by van der Waal forces or pressure sensitive adhesives (PSA). More practically, FS traces can be designed in different layouts with adjustable resistance-based responses for multi-functional sensing, including body temperature [4], biopotential [36], and auxiliary strain sensing [31,37]. Furthermore, the combination of FS design with a pre-strained substrate can significantly improve the stretchability of the device [38,39].

Human skin is a highly complex biological material that insulates and protects internal organs from the external environment. It can be described as a multilayered structure comprising the epidermis, dermis, and hypodermis [17]. Epidermis (average thickness of 40–50 μm) is the outermost layer of skin. The outermost layer of the epidermis is the stratum corneum, which is the main reason that the lifespan of skin-wearable devices is limited to 2 weeks due to the exfoliation of old cells [8]. The dermis layer, which is beneath the epidermis accounts for 90% of the thickness of the skin (1.5 to 4 mm) [40]. The dermis regulates body temperature and supplies oxygen and nutrients to the skin via blood vessels [40]. Sweat glands located throughout the body adjust body temperature by bringing water to the skin surface where it evaporates through pores. This process can produce up to 2 L of sweat per hour, providing a wealth of information about the metabolism [40]. Lymph vessels in the dermis contain infection-fighting cells from the immune system and play an important role in wound healing by destroying infecting or invading organisms [41,42]. Moreover, nerve endings that exist in the dermis layer transmit sensations, such as pressure, pain, and temperature to the brain for interpretation [40]. The hypodermis layer is the innermost layer of the skin, through which the blood vessels, nerves, lymph vessels, and hair follicles also pass. Since the light transmittance of human skin varies with wavelength, systolic–diastolic signals, and blood oxygen saturation can be detected from the blood vessels. High-sensitivity pressure sensors can record similar arterial systolic–diastolic signals due to the softness of the skin. Another signal that can be obtained from the skin surface is biopotential, which comes from the muscle layer beneath our skin [43]. Therefore, methods that detect electrophysiological signals, such as electroencephalography (EEG), electromyography (EMG), and electrocardiogram (ECG), can be used to monitor brain, heart, and muscle activity, respectively.

Skin-accessible health information can be obtained by an electronic sensor, which generally refers to devices that convert detected input signals into electrical outputs [44]. Based on the physical understanding of the signal domains, in 1989, Göpel et al. introduced the classification of transduction principles, which provides a method to visualize sensing principles [45]. While modern sensors can be more complex due to the involvement of multiple sensing principles and can be classified according to applications, specification, etc., this review selects the primary input energy form for classification in terms of material properties and selection.

So far, the signals that can be transmitted and processed from the skin are divided into five types of sensors: thermal (of temperature), electrical (of neural electricity), radiant (of photoelectricity), mechanical (of pressure) (all of which are found in Table 1), and electrochemical (of sweat).

Table 1. Summary of skin-wearable devices.

Sensor Classification	Sensing Mechanism	Measurement Signal	Conductive Material	Signal	Measure Locations	Treatment	Substrate	Refs
Neural electrical sensor	Electrode	ECG	CNT	Voltage	Chest	Cardiology	PEIE/CNT/PDMS	[46]
		ECG	Commercial 3M electrode	Voltage	Chest and wrist	Cardiology, brain activity, muscle movement	PDMS	[47]
		ECG	Ag microparticles	Voltage	Chest, arm, scalp	Cardiology	PDMS	[5]
		ECG, EMG	Carbon nanofillers	Voltage	Wrist, stomach, ankle	Cardiology, muscle movement	PDMS	[30]
		ECG, EEG, EMG	Cr/Au FS	Voltage/frequency	Arm, neck, forehead, chest, leg	Cardiology, brain activity, muscle movement	Modified silicone (Smooth-on)/PVA	[36]
		EMG	Au FS	Voltage	Arm, prosthetic	Muscle movement, robotic arm control	Ecoflex (Smooth-on)/PVA	[37]
		EEG	Au FS	Voltage	Ear	Brain activity	silicone elastomer/PVA	[48]
		ECG	Au/Ti FS	Voltage	Neck, chest	Cardiology	Adhesive PDMS	[49]
		ECG, EEG, EMG	Cr/Au FS	Voltage	Back, arm, scalp	Cardiology, brain activity, prosthetic control	Silicone bylayer: Adhesive silicone (RT GEL 4642, Bluestar), Ecoflex (00-30 Smooth-on)	[50]
		ECG, EMG	Cr/Au FS with NdFeB	Voltage	Chest, arm, cheek	Cardiology, muscle movement	Adhesive Bluestar Silicones	[51]
		ECG, EEG, EMG	PEDOT:PSS	Voltage	Chest, arm, scalp	Cardiology, muscle movement, brain activity	PEDOT:PSS/waterborne polyurethane (WPU)/D-sorbitol blend	[2]
Thermal sensor	Thermal resistance		Cu	Resistance	Arm	Wound healing	Ecoflex	[52]
			Pt	Resistance	Skin	Body temperature	Modified silicone (Smooth-on)/PVA	[36]
			Au	Resistance	Arm	Body temperature	Ecoflex, (Smooth-on)/PVA	[37]
			Au	Resistance	Skin	Temperature beneath 6 mm of skin surface	Ecoflex	[53]
			Ni-NiO-Ni	Resistance	Facial surface	Respiration temperature	PET	[54]
	Temperature	PEDOT:PSS	Resistance	Skin/hand	Body temperature	PDMS	[55]	
		Cr/Au FS	Voltage	Wrist	Blood flow	Ecoflex	[56]	
	Thermocouple	Cr/Au FS	Voltage	Cheek	Vascularization, blood flow, stratum corneum thickness, hydration	Ecoflex 00–30	[57]	
	Diode thermal sensor	PIN diode sensor	Voltage	Skin, palm	Body temperature	Silicone elastomer/PVA	[4]	

Table 1. Cont.

Sensor Classification	Sensing Mechanism	Measurement Signal	Conductive Material	Signal	Measure Locations	Treatment	Substrate	Refs
Mechanical sensor	Photodetector	PPG, SO ₂	P3HT: PCBM	Voltage	Fingertip	Cardiology	Parylene	[58, 59]
		Blood pulse	PEDOT: PSS	Current	Wrist	Cardiology	PDMS	[60]
	Piezoresistivity	Blood pulse	Graphene oxide	Resistance	Wrist, fingertip, chest	Cardiology, respiration states	PDMS	[61]
		Blood pulse, static tremor	Graphene oxide	Current	Wrist, fingertip	Cardiology, Early-stage Parkinson's disease	Polyurethane sponge	[62]
		pulse rate	EGaIn	Voltage	Wrist	Cardiology	PDMS	[63]
	Capacitance	Pulse rate, PWV	Mg/Fe	Capacitance	Wrist, carotid artery, skin above femoral artery	Cardiology, arterial stiffness	PHB/PHV	[64]
		Pulse rate, muscle movement	PEDOT:PSS/Mxene/P(VDF-TrFE)	Capacitance	Wrist, arm, dermal area of eye and throat	Cardiology, Early-stage Parkinson's disease	PDMS	[65]
		Pulse rate, physiologic pressure	Cu	Capacitance	Wrist, Intracranial (of mice)	Cardiology, intracranial pressure	SBS	[66]
		Pulse rate, PWV	P(VDF-TrFE)/PEDOT:PSS	Voltage	Wrist, neck	Cardiology, arterial stiffness	PEN	[67]
		Pulse rate, PWV	PZT	Current	Wrist, neck,	Cardiology, arterial stiffness	Ecoflex 00-30	[68]
		Skin modulus	PZT	Voltage	pathologies of skin regions	Dermatology	Ecoflex 00-30	[69]
		Pulse rate	PDA/BTO/PCVF	Voltage	Wrist, dermal area of throat	Cardiology	PET	[70]
	Piezoelectricity	Ultrasound images	Commercial ultrasound prob	Voltage	Neck, chest	Images of lung, diaphragm, heart, and stomach	Bioadhesive hydrogel elastomer couplant	[32]
		Ultrasound images	PZT-5H	Voltage	Chest	Images of heart	SEBS	[71]

3. Electrical Signals Related to Neural Activity

3.1. Neural Electrical Signal Monitoring Mechanism

Biological fluid activities that present electrolytes generate potentials. The potentials can be recorded with a direct electrical contact to skin or through capacitive coupling. The exploration of these activities and the molecular and cellular processes that control their signaling is called electrophysiology, a branch of neuroscience [72]. There are three main types of electrophysical signals that can be obtained non-invasively from skin: electrocardiology (ECG) for heart activity, electroencephalography (EEG) for brain activity, and electromyography (EMG) for muscle movement.

The ECG signal is an electrical signal that travels through the heart by a series of depolarizations and repolarizations in cardiac cells [73]. This electrical signal is generated by an impulse from the depolarization of the atria (upper chamber of the heart) and presents

as the P-wave of ECG. Then, the electrical current travels to the lower chamber of the heart, causing the depolarization of the ventricular cardiac muscle and presenting as QRS-complex. The P and QRS complexes have differences in amplitude due to differences in the muscle mass of the atria and ventricles. Repolarization then occurs in the opposite direction as the relaxation of the ventricular cardiac muscle and presents as T-wave (Figure 1). This signal includes an AC potential range from 0.5 to 5.0 mV (1 mV peak-to-peak), a DC potential component up to ± 300 mV caused by impedance between the skin and the device, and a bandwidth range of 0.5–100 Hz [74]. Although ECG signals can be simply obtained by 2 electrodes, the clinic-standardized ECG uses 10 electrodes placed throughout the body based on Einthoven's triangle and records the signals from 12 different directions [75,76]. Viewing the heart from unique angles in each direction provides the opportunity to localize lesioned areas [77]. The abnormality in ECG relates to cardiovascular diseases, such as arrhythmia [78], ischemia [79], hypertrophy [80], and aneurysm [81]. For conventional ECG recordings, the potential changes in 12 different directions in 10 electrodes are measured [76]. One common placement of the electrodes is based on Einthoven's triangle, which is an imaginary triangle drawn around the volume of the heart [75]. Each apex of the triangle represents where the body's composition, with respect to the heart, connects electrically with the limbs. The twelve leads are made up of three bipolar and nine monopolar leads [76]. There are three main leads responsible for measuring the electrical potential difference between arms and legs [74]. The three bipolar leads measure the electrical potential between the right and left arm (lead I), the right arm and the left foot (lead II), and between the left arm and the left foot (lead III). In all ECG lead measurements, the electrode connected to the right leg is considered the ground node. An ECG signal will be acquired using a biopotential amplifier and then displayed using instrumentation software, where a gain control will be created to adjust its amplitude. To minimize the size of the portable device, the smaller devices often rely on only two electrodes to deliver a single lead [82]. It is worth mentioning that cardiac activity includes muscle activity, a galvanic potential of arteriole vs. venule blood flows components, and a galvanic potential dynamic in the blood peripheral vessels.

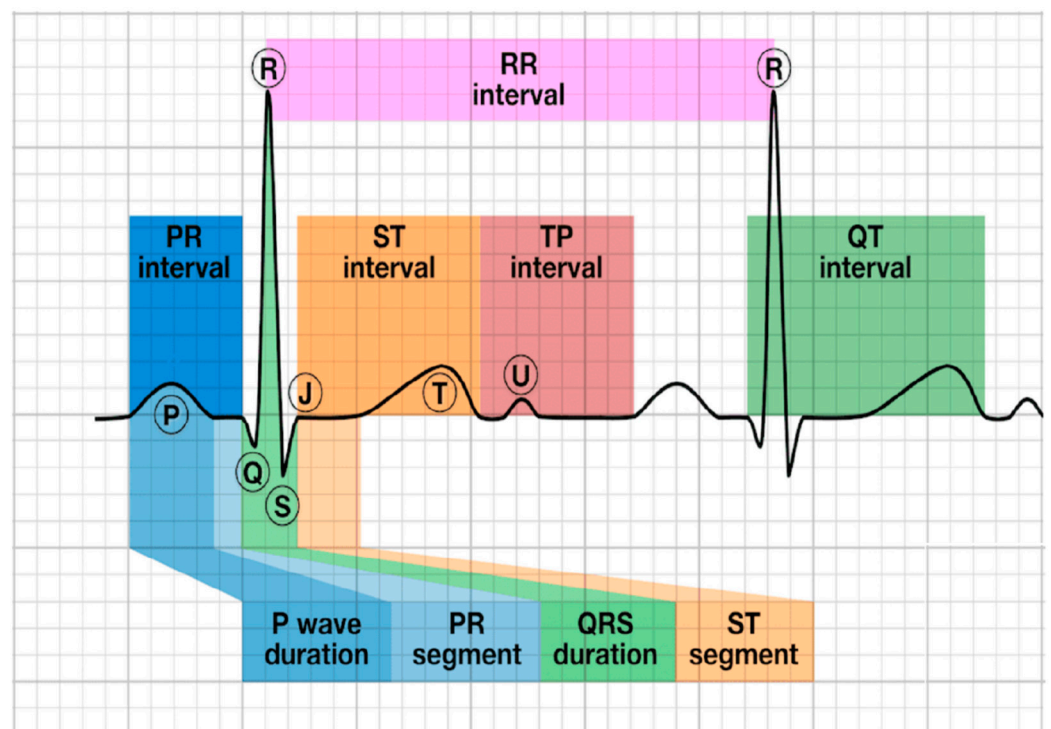


Figure 1. Schematic of ECG signal caused by depolarization and repolarization of the heart. (Reprinted/adapted from reference [83]).

EEG detects the postsynaptic potential of pyramidal cells in the epithelial cortex of the scalp [84,85]. The normal activities of a living individual can be divided into five EEG patterns, namely, Delta (deep sleep), Theta (under emotional pressure), Alpha (relaxed state), Beta (alert state), and Gamma (perceptual activity) [86]. With increasing activity, the frequency of EEG increases (from 0.3 to 50 Hz) and the amplitude decreases (from 200 to 5 μV) [86]. In normal brain activity, cells are activated asynchronously and deliver small potentials to the scalp. Neurological disorders, such as epileptic seizure, manifest as sudden synchronous and repetitive discharge by a group of simultaneously activated cells and produce high EEG amplitudes [85]. Therefore, EEG is commonly used to analyze neurological and psychiatric disturbances [87], such as brain disorders [88], epilepsy [89], brain tumors [90], brain injuries [91], and early stages of Parkinson's disease [92]. An EEG system consists of electrodes, amplifiers, filters, and a recording unit [86]. Electrodes are usually placed on conductive gel, following the international 10–20-based system. The electrical signal received from the electrodes needs adequate amplification followed by the removal of noise, using an amplifier and a filter, respectively. An analog-to-digital converter (ADC) is employed to convert the signal into digital form before feeding it to a computer for analysis and storage.

EMG is used to detect muscle movements and the nerve cells that control movements. Electrical signals of muscle movements are generated by the motor cortex of the brain, are transmitted to the spinal cord, and are finally sent to the relevant muscles via motor neurons [93]. During this process, upper motor neurons transmit information to lower motor neurons, which innervate muscle movement by releasing calcium ions and causing muscle tension [93,94]. The depolarization involved in the process provides an electrical current difference that can be detected by small needle electrodes on the skin. The measured electric signal can be less than 50 μV and as high as 30 mV, depending on different muscles [95]. Myopathic muscles result in more complex signals than normal muscle movement because they are generally smaller and need to be activated at a higher firing rate. In contrast, the signals of neurogenic disorders are less complex due to the fewer number of them needed to be activated at equivalent muscle activations [96]. Thus, diseases such as myopathy [97], neurogenic muscle wasting and weakness [98], abnormalities [99], radicular pathology [100], and motoneuron disease can be detected and diagnosed by EMG [101]. During an EMG test, small needles (electrodes) are inserted through the skin into muscle. The electrical activity picked up by the electrodes is then displayed on an oscilloscope. An audio-amplifier is used to hear the activity. EMG measures the electrical activity of muscle during slight contraction and forceful contraction. EMG clinical examinations have, thus, been extended for the detection of other diseases, including myopathy, neurogenic muscle wasting and weakness, abnormalities, radicular pathology, motor neuron disease, etc [100]. Furthermore, the EMG signals from muscle contractions of the biceps or triceps are commonly used for robotic control prosthetics, and machine-assisted living [8].

3.2. Neural Electrical Signal for Skin-Wearable Devices

Current clinical applications of ECG, EEG, and EMG use conductive gels (Ag/AgCl), which create less impedance between the skin and the electronic devices. The drying properties of conductive gels prevent long-term monitoring, which some sudden illnesses, such as epileptic seizure that does not continue to trigger epileptic discharges, require to document abnormalities [102]. An alternative is to use dry electrodes; however, dry electrodes suffer from high impedance and low signal-to-noise ratios (SNR), and create uncomfortable skin–device contact [103]. Since dry electrodes create weak signals and are susceptible to noise, it is imperative to explore the new electrophysical skin-wearable sensors with excellent mechanical properties for long-term attachment purposes. As summarized in Table 2, until now, proposed skin-wearable sensors for biopotential are utilizing two main strategies for conformal skin contact: van der Waals forces, adhesion, and pressure sensitive adhesion (PSA).

Table 2. Summary of electrophysiology sensors.

Skin-Contact Strategy	Skin-Contact Method/Material	Electrode Material	Impedance	Treatment	Refs
Van der Waals forces	Hydrogel electrode	Ag/AgCl	20 k Ω (50 Hz)~75 k Ω (100 Hz)	ECG	[104]
	CNT/PDMS	CNT	~100 k Ω (100 Hz)	ECG	[105]
	CNT/PEIE/PDMS	CNT	~145 k Ω (100 Hz)	ECG	[46]
	PDMS /in gecko-inspired micropillar structure	Commercial medical 3M electrode	N/A	ECG	[47]
	Ag particles in PDMS/ in micropillar structure	Ag	50 k Ω (10 Hz)	ECG, EEG, EMG	[5]
	hybrid nanofiller in PDMS/ in gecko-inspired micropillar structure	1-D CNT and 2-D graphene nanopowder	N/A	ECG	[30]
	Silicone elastomer/PVA	Cr/Au FS	N/A	ECG, EEG, EMG	[36]
	Ecoflex (Smooth-on) /PVA	Au FS	N/A	EMG	[37]
	Silicone elastomer/PVA	Au FS	N/A	EEG	[48]
Pressure sensitive adhesive layer	CNT/Adhesive PDMS	Au/Ti/polyimide FS	241 k Ω (40 Hz)	ECG	[49]
	Silicone adhesive	Cr/Au FS	30 k Ω (30 Hz)	ECG, EEG, EEG	[50]
	Adhesive Bluestar Silicones / ferromagnetic dipole	Cr/Au FS	<100 k Ω (10 kHz)	ECG, EEG, EMG	[51]
	PEDOT:PSS/ waterborne polyurethane (WPU) /D-sorbitol	PEDOT:PSS	82 k Ω cm ² at 10 Hz	ECG, EEG, EMG	[2]

Van der Waals forces include attraction and repulsion between surfaces, atoms, molecules, and intermolecular forces. Despite their short range (0.2–40 nm), van der Waals forces play an important role in microscale and nanoscale [106]. The devices that attach on the skin via van der Waals forces are capable of obtaining electrophysical signals on various areas of the body even under strain from different device structures and materials. Such dry bonding typically requires the participation of a low modulus and/or an ultra-thin gauge elastomer matrix. For example, carbon nanotube (CNT)-mixed polydimethylsiloxane (PDMS) was used to substitute the commercial Ag/AgCl gel for dry contact with skin [105]. Later research introduced ethoxylated polyethylenimine (PEIE) in PDMS/CNT composites to reduce impedance between the electrode and the skin [46]. The nature-inspired gecko tow pad structure further enhances the adhesion by replicating the columnar microstructure and fabricating it with silicone elastomer for strong and reversible adhesion between surfaces. The commercial conductive gel can be then substituted by this structure combined with commercial ECG electrodes [47]. The device is capable of continuously acquiring data for 48 h on flat or curved surfaces (chest and wrist) [47]. Silver (Ag) microparticles have been mixed with PDMS to form pillar structures, which exhibited an impedance of 50 k Ω cm² at 10 Hz and a readable high-fidelity ECG during movements [5]. Adding hybrid nanofiller (1D carbon CNT and 2D graphene nanopowder at a ratio of 1:9) to PDMS exhibits superior stretchability of over 100% and high conductivity, with a resistivity of less than 100 Ω cm, which is comparable to commercial ECG applications (Figure 2a–c) [30]. Van der Waals forces between the skin and the device can be achieved using low modulus silicone elastomers and sacrificial polymers. The sensing element consists of Cr/Au FS traces that are sandwiched between spin-coated polyimide and is accomplished by photolithography and dry etching. This method was first proposed in 2011 when researchers achieved conformal attachment of PI-Cr/Au-PI

traces using low-modulus silicone (Figure 2d–f) [36]. The [polyvinyl alcohol (PVA)] is used as a temporary support because the water-soluble nanofibers allow it to stick on the skin via van der Waals forces. The device is stretchable with a repeatable strain of approximately 30%. By incorporating FS traces, the device is capable of multifunctional operation not only for ECG, EEG, and EMG but also for body temperature, LED and photodetectors, and wireless power.

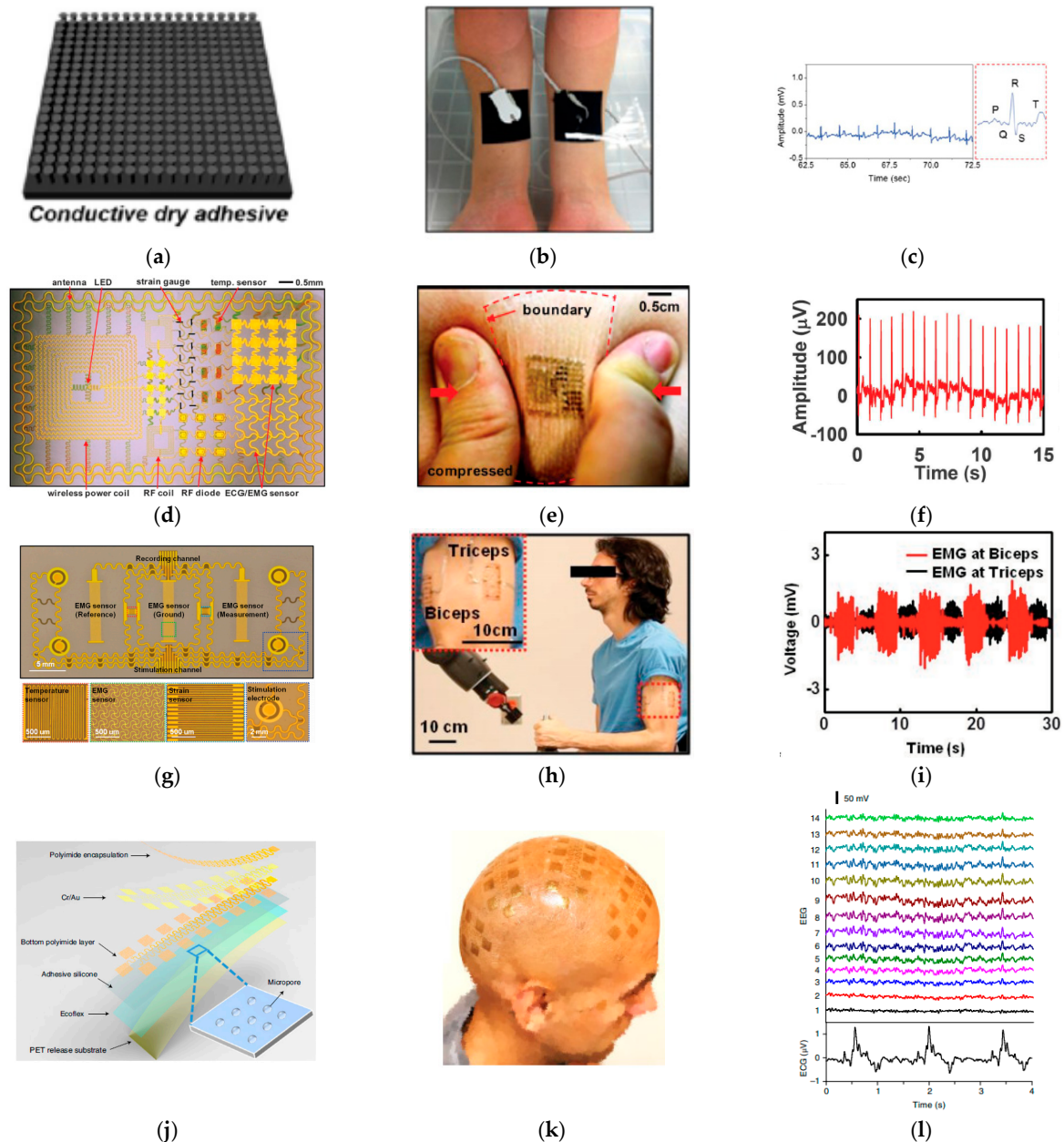


Figure 2. Images of skin-wearable electrophysical devices that are attached on skin based on van der Waals forces (a–i) and pressure sensitive adhesives (PSA) (j–l). (a) Schematic diagram of gecko-inspired micropatterns with nanocomposite mixed in elastomer matrix. (b) The device is capable of continuous monitoring on the forearm under water immersion conditions with (c) ECG signal. (d) Schematic diagram of multifunctional FS-based device. (e) The device on skin under compression. (f) Example of an ECG measurement from chest attachment. (g) Schematic diagram of the device design for EMG monitoring and simulation. (h) The devices on biceps and triceps for robotic arm control. (i) Voltage traces for EMG at Biceps and Triceps. (j) Schematic diagram of device layers. (k) Device on a head. (l) EEG traces.

(i) Separate EMG signals from the two devices during flexion and extension of the robot elbow angle. (j) Schematic diagram of layers of the large-area multi-channel flexible and stretchable device. (k) Conformal contact between the subject's scale and the device with 68 electrodes for EEG detection. (l) The EEG and ECG signals obtained with standard digital filtering techniques. (Reprinted/adapted from reference [30]; Reprinted/adapted with permission from reference [36], Copyright 2011, Science; Reprinted/adapted with permission from reference [37], Copyright 2015, Advanced Materials; Reprinted/adapted with permission from reference [50], Copyright 2019, Nature Biomedical Engineering).

The van der Waals forces approach can also be utilized for EMG signals and simulation. A sensor combined with an actuator employs a PI-Au-PI trace-like design on a water-soluble PVA substrate (Figure 2g–i) [37]. Here, the FS traces made of the same material with different geometries are used to detect EMG, temperature, and strain. The resistance-based results are adjustable to compensate for transverse sensitivity and eliminate the effects between different working elements. The device expands the scope of applications through the participation of actuators that receive electrical input and execute the movement of the robotic arm by placing two devices on the triceps and biceps, respectively. Inducing muscle contractions offers an opportunity for prosthetic control through perceptual feedback and stimulation. Additionally, van der Waals force attachments are eligible for complex textures in small areas, such as auricula, which require extremely bendable electronics. The attached tripolar concentric ring layout sensor with a PVA water-sacrificial layer can be laminated on the auricle to not only obtain long-term EEG signals but also track letter spelling by steady-state visually evoked potentials (SSVEP) [48]. Since each visual target flickers at a unique frequency, the algorithms based on canonical correlation analysis (CCA) are able to classify the subject's desired character for test spelling.

Another strategy for skin-to-device contact is the application of pressure sensitive adhesives (PSA), which are the viscous substrate that achieve conformal contact by electrostatic forces. Similar to van der Waals forces in essence, electrostatic interactions are attractive or repulsive forces between two surfaces caused by the opposite or the same charges [107]. The difference between them is that electrostatic force has a larger value and a longer dominant distance of a few micrometers [108,109]. It is worth mentioning that even when SPA tape is able to hold two surfaces together by electrostatic forces, van der Waals forces are still involved when two subjects are close enough. If the applied pressure is inadequate, the bonding faults, such as bubbles or detachment, may exist and affect adhesion [110]. Adhesion and flexibility contribute to PSA for wearable devices to form conformal contact even under large strain. In 2014, the skin-wearable ECG patch was made of mixing CNT with adhesive polydimethylsiloxane (aPDMS) as the adhesion layer for Au/Ti/polyimide FS to form a triangle structure with three leads and to provide ECG signals from three directions [49]. An adhesive force of 1.1 N cm^{-2} ensures the firm skin attachment with an impedance of $241 \text{ k}\Omega$ at 40 Hz . The device obtained comparable results to the commercial Ag/AgCl electrodes when attached to the subject's chest. PSA layers enable large-area multi-channel devices for biopotential detection (Figure 2j–l) [50]. In this study, adhesive silicone was used as the interface between the skin and the device. The micropores in the adhesive silicone provide a highly breathable interface, which is the result of micropores poly (methyl methacrylate) (PMMA) that is embedded before curing and removed after curing by acetone. The device can measure reinnervated muscle movements simultaneously in eight channels when mounted on the amputated upper limb. Clear signals for ECG and EEG are obtained by using standard digital filtering techniques. Conformal electronics can further monitor these signals during functional magnetic resonance imaging (fMRI) and provide additional information on physical and psychological states [111]. Another way to enhance the adhesion force is to use an auxiliary bilayer consisting of a ferromagnetic layer and adhesive silicone with conductive FS traces [51]. The obtained device with an SNR of 8.2–13 is suitable for clinical applications, such as ECG, EEG, and EMG. In addition, conductive materials can also be mixed with structural materials to form the PSA layer directly. Using poly(ethylenedioxythiophene):poly(styrenesulfonate) (PEDOT:PSS) mixed

with waterborne polyurethane (WPU) and D-sorbitol, the stretchable electronic with an adhesive force of 0.4 N cm^{-1} and a low impedance of $82 \text{ k}\Omega \text{ cm}^2$ at 10 Hz was formed [2]. The device can be attached to the skin to detect the clear signals of ECG, EMG, and EEG.

4. Thermoelectrical Signal Measurement

4.1. Thermoelectrical Signal Monitoring Mechanism

Body temperature, a consequential by-product of heat energy metabolism, has been widely used as an index of illness since 400 BC [1,112,113]. The core energy of the body must be emitted to the surrounding environment to avoid overheating [114]. Heat transfer properties of the skin reveal changes relevant to human physiology, such as skin state, activity, and thermoregulation [57]. The heat production rate and the heat lost rate are maintained in a balance through radiation, convection, conduction, and evaporation, resulting in body temperature falling within a fairly narrow range from 36 to $38 \text{ }^\circ\text{C}$ [112,114]. Lost control of body temperature can lead to impairments of physiological function, lost consciousness, and/or death [112].

Body thermal detection has been widely used in the medical monitoring of inflammatory response, a defense mechanism of the immune system that evolved in higher organisms to protect them from infection and injury [115]. The purpose of inflammation is to locate and eliminate harmful substances and damaged tissue components, allowing the infected area of the wound to begin to heal [116]. The constriction of capillaries draws blood away from the infected area, causing engorgement of the capillary network, which increases blood flow and temperature in the wound healing area. Therefore, thermography, a process in which a thermal imager captures the images of infrared radiation emitted from the object, enables the localization and monitoring of the inflammation area and wound processes. In addition, thermal detection can prevent the patient from suffering a stroke or heart attack if such inflammation occurs in carotid arteries [117]. The evidence also suggests that the lesioned area of breast cancer releases more heat than the surrounding areas, which could be caused by a number of possible explanations, including angiogenesis, nitric oxide, inflammation, and estrogen [118,119]. Thermography was used as an early preclinical diagnosis of breast cancerous lesions in 1956, and was approved by the FDA as a breast risk assessment tool in 1982 [120,121]. Finally, high skin temperature, especially during exercise, is associated with dehydration, which leads to cardiovascular and thermoregulatory systems under stress [112]. High skin temperature also results in plasma loss, which is caused by decreases in cutaneous capillary resistance due to profound cutaneous vasodilation [122].

4.2. Thermoelectrical Signal for Skin-Wearable Devices

Conventional skin temperature detection either uses simple single-point contact measurements or sophisticated infrared digital cameras for spatial imaging. Point contact methods are cost-effective and convenient for diseases such as systemic fever; however, it is hard to detect diseases that only occur in specific areas of the body, such as inflammation and breast cancer. Infrared spatial thermography offers an accurate solution for imaging, but it is expensive, incapable of continuous long-term monitoring, and requires the immobilization of patients [4]. The skin-wearable devices effectively solve this dilemma using three types of thermoelectric sensors: a resistance temperature sensor, a thermocouple, and a diode thermal sensor.

Resistance temperature sensors are made of metal and, therefore, have a positive temperature coefficient and lower sensitivity [123]. The temperature depends on resistance:

$$R = R_0 \left(1 + AT + BT^2 \right) \quad (1)$$

where R_0 is the resistance at the reference temperature (usually $0 \text{ }^\circ\text{C}$), and A and B are the coefficients that depend on the different metals applied. The metals used most often are platinum (Pt), nickel (Ni), and copper (Cu). Cu has been built into a resistance thermal sensor to monitor wound healing by utilizing a 3- μm -thick fractal layout designed in six

sensing elements for an epidermis electronics system (EES) (Figure 3a–c) [52]. Having six sensors provides accessibility for spatial records of temperature and thermal conductivity. Polyimide layers and Cu traces minimize the bending strains. The encapsulated traces are transferred to a silicone membrane to realize a waterproof device. The results show that the electrical resistance change is capable of temperature measurement with a precision of ~50 mK in lab and ~200 mK in clinical testing. The device was laminated on a cutaneous wound from day 1 to day 30 after surgery to monitor the temperature change in the skin surface of the forearm. The inflammatory phase of wound healing can be detected when the thermal conductivity changes on day 3. Similar resistance-based metal filamentary serpentine designs also use Pt and Au as the sensing array for temperature sensing, with performances comparable to that of an infrared camera [4,36]. Human skin exhibits large variations in thermal properties. A Au coil geometry device has been reported to measure temperature up to 6 mm beneath the skin surface by finite element analysis (FEA) [53]. NiO has been used for body temperature sensing due to its relatively large negative temperature coefficient (NTC), which exhibits a simple structure and high temperature sensitivity [54]. In the study, the NiO metallic nanoparticles coated layer was irradiated with a laser to fabricate Ni-NiO-Ni structures with tens-of-micrometer-wide NiO channels. The final device presents a response time of 50 ms, which could be attributed to the 25 μm -thin PET substrate. The respiration temperature during exercise can be detected when the device is attached to the front of the nasal cavity. In addition, a metal and metal oxide, PEDOT:PSS, has also been used for temperature sensing by applying pre-strain to PDMS substrates [55].

A thermocouple measurement is based on the interaction between thermal energy and electrical energy and is associated with the Seebeck effect [123]. The Seebeck effect is the phenomenon of current flowing around a loop and/or electric potential across an open loop connecting two different types of metals with a temperature difference [124]. The performance of a thermocouple is described as the metals' figure of merit:

$$ZT = S^2\sigma T/\kappa \quad (2)$$

where S is the Seebeck, σ is electrical conductivity, T is absolute temperature, and κ is thermal conductivity [125]. High electrical conductivity and the Seebeck coefficient, along with low thermal conductivity, contribute to the performance of the thermoelectric materials [126]. A chromium/gold (Cr/Au) filamentary serpentine structure has been designed for the epidermal sensor that maps macrovascular and microvascular blood flow beneath a targeted area of skin (Figure 3d–f) [56]. The 3-mm-diameter device contains 1 central actuator (10-nm Cr/100-nm Au) and 2 rings from the sensors (10-nm Cr/100-nm Au) for spatial response. During the sensing process, the actuator provides a constant thermal source at the surface of the targeted vessel. The two sensors rings provide the result of the thermal distributions with a precision of 0.01 $^{\circ}\text{C}$. An additional sensor outside the rings is served to detect and compensate the temperature changes of the surroundings. The sensor is supported, and it is adhered to the skin, by silicone substrates. The high gas permeability ($2 \text{ g h}^{-1}\text{m}^{-2}$) of the silicone base and the low thermal mass ($0.2 - 5.7 \text{ mJ cm}^{-2}\text{K}^{-1}$) of the complete device ensure the minimal perturbation of the skin temperature. The changes in blood flow were able to be recorded during hyperemic reaction induced occlusion and reperfusion on the skin surface of the subject. Furthermore, the correlation of skin temperature detected by the ultrathin Cr/Au thermocouple, which recorded vascularization, blood flow, stratum corneum thickness, and hydration level, has been reported [57].

A diode thermal sensor is attributed to the nonlinear asymmetric diffusion current in a p-n junction with two different materials that have different temperature-dependent thermal conductivities [127–129]. Adding an intrinsic layer (i-region) sandwiched between the p-layer and the n-layer constructs a p-i-n (PIN) diode, which has a wide intrinsic layer that provides low and constant capacitance, high breakdown voltage in reverse bias, and a variable attenuator [123]. Recent research has helped design a multiplexed sensor array based on PIN diodes formed by the patterned doping of Si nanomembranes for a skin-wearable thermal sensor (Figure 3g–i) [4]. The small thickness of the device results in

a thermal mass of $7.2 \text{ mJ cm}^{-2} \text{ K}^{-1}$ and a thermal inertia of $\sim 500 \text{ W s}^{1/2} \text{ m}^{-2} \text{ K}^{-1}$. The PIN system includes 64 sensors (each with a size of $100 \text{ }\mu\text{m}$ by $200 \text{ }\mu\text{m}$) with 16 external connections. The resolution of the spatial image can, thus, be improved by the scalability of microfabrication. This sensing array displays the precision of $\sim 8 \text{ mK}$ in lab and $\sim 14 \text{ mK}$ in a hospital setting at 0.5 Hz .

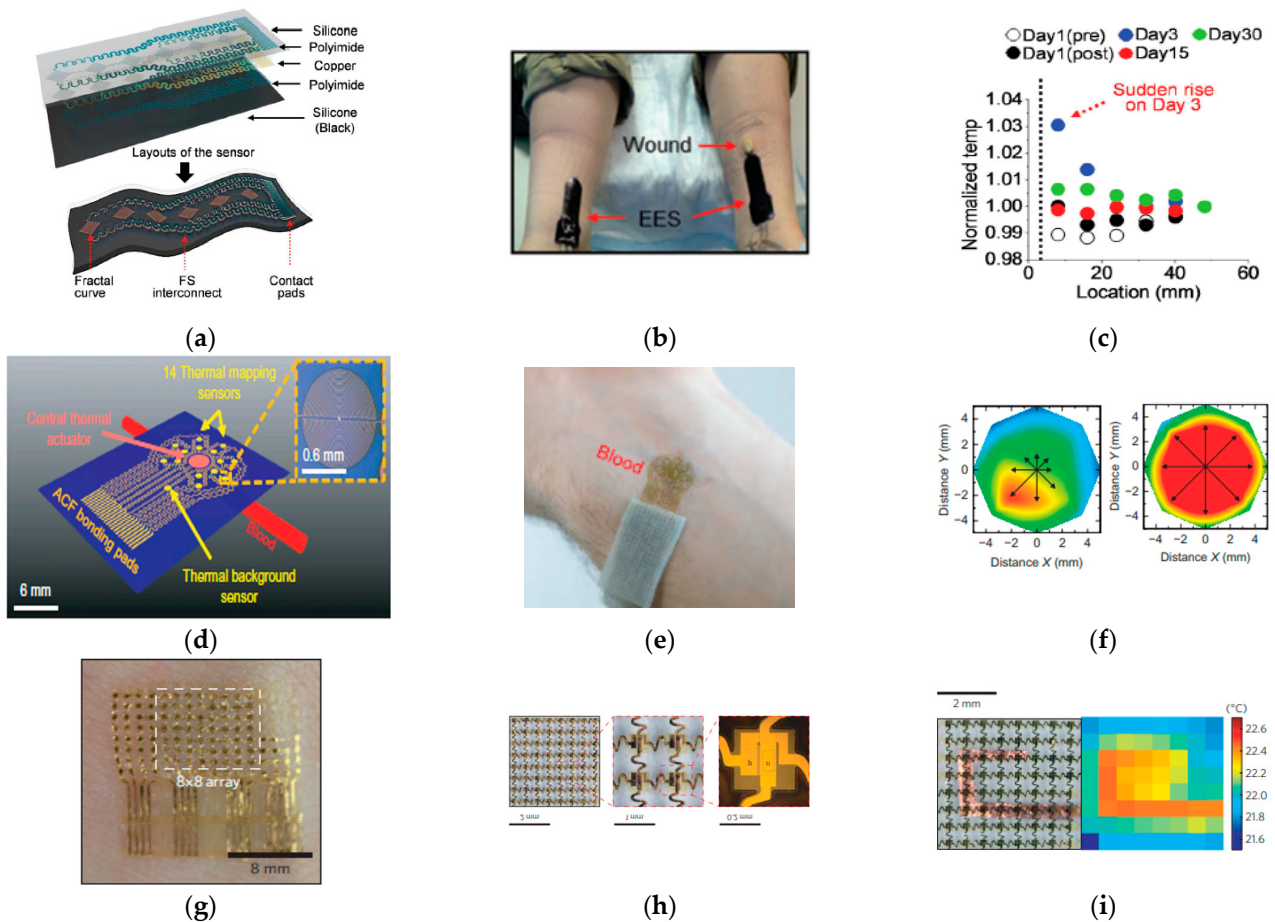


Figure 3. Images of skin-wearable thermoelectrical devices with spatial thermography. (a) Schematic of the multilayer structure of the resistance thermal sensor with six sensing elements of fractal curves and interconnecting filamentary traces. (b) Devices mounted on wound. (c) Temperature distribution recorded with 6 sensors spanning 45 mm in lateral direction starting near the wound site. (d) Schematic illustration of the thermocouple layout for an actuator and 14 thermal mapping sensors. (e) Placement of the sensor on human skin. (f) An example of the spatial thermography at peel flow (left) and occluded flow (right). (g) Optical image of an 8 by 8 Si nanomembrane diode sensor array mounted on the skin. (h) Optical images of the 8 by 8 Si nanomembrane diode sensor array (left) and magnified views of a single sensor (center and right). (i) Optical image of the device mounted on a heated Cu element (left) and measured distribution of temperature (right). (Reprinted/adapted with permission from reference [52], Copyright 2014, Advanced Healthcare Materials; Reprinted/adapted from reference [56]; Reprinted/adapted with permission from reference [4], Copyright 2013, Nature Materials).

5. Photoelectrical Signal Measurement

5.1. Photoelectrical Signal Monitoring Mechanism

The human body is light transparent, and this natural property has been used to detect pulsating arterial blood since World War II [130]. Light passing through our body is attenuated and absorbed by a pulsating component, such as blood passing through the arteries and arterioles, and a non-pulsating component, such as venous blood, bones, and other tissues [58]. The pulsating part is considered a DC component (noise signal), and the

non-pulsating part is treated as an AC signal. The systolic is caused by a forward-going pressure wave that transmits from the left ventricle to the peripheral tissue, and the diastolic is the result of the pressure wave transmitting from the aorta to small arteries in the lower body [131]. The recorded systolic–diastolic cycle is shown in Figure 4a. This continuous change is recorded by a light source and a photodetector (PD) via PPG. According to the PPG signals in different areas of the body, the abnormality of blood vessels can be located [132]. Because PPG is caused by heart contraction and blood flow, the pulse transit time (PPT) exists between the systolic and diastolic peaks. It represents the propagation time of the pressure wave from the subclavian artery to the apparent reflection site and back to the subclavian artery [131,133]. The artery stiffness (SI), which reflects blood flow velocity, is proportional to the ratio between the subject's height (h) and PPT [134]. The researchers observed that 98% of the patients with arteriosclerosis in the study had a diminution or disappearance of the dicrotic wave, while the health volunteers present ill-defined dicrotic peaks [135]. In addition, first and second derivative PPG signals are also related to the carotid artery [136], age [137], blood pressure [138], the risk estimation of coronary diseases [139], and the presence of atherosclerotic disorders [140]. Commonly used light sources for PPG are green light and red/near-infrared light. Green light is largely used in a commercial daily reflectance mode due to its great signal-to-noise ratio and ability to resist motion artifacts; however, it can be absorbed by melanin, resulting in an increase in a variation of accuracy [141,142]. Red/near-infrared light has been used for medical purposes because the human body does not absorb much red light and because it can go deeper into multiple tissue layers for biometric signals; however, red/near-infrared has a lower signal-to-noise ratio and susceptibility to motion artifacts [142]. It is worth mentioning that water begins to absorb light with a wavelength greater than 940 nm, and, therefore, the maximum wavelength of PPG is generally 940 nm [143,144].

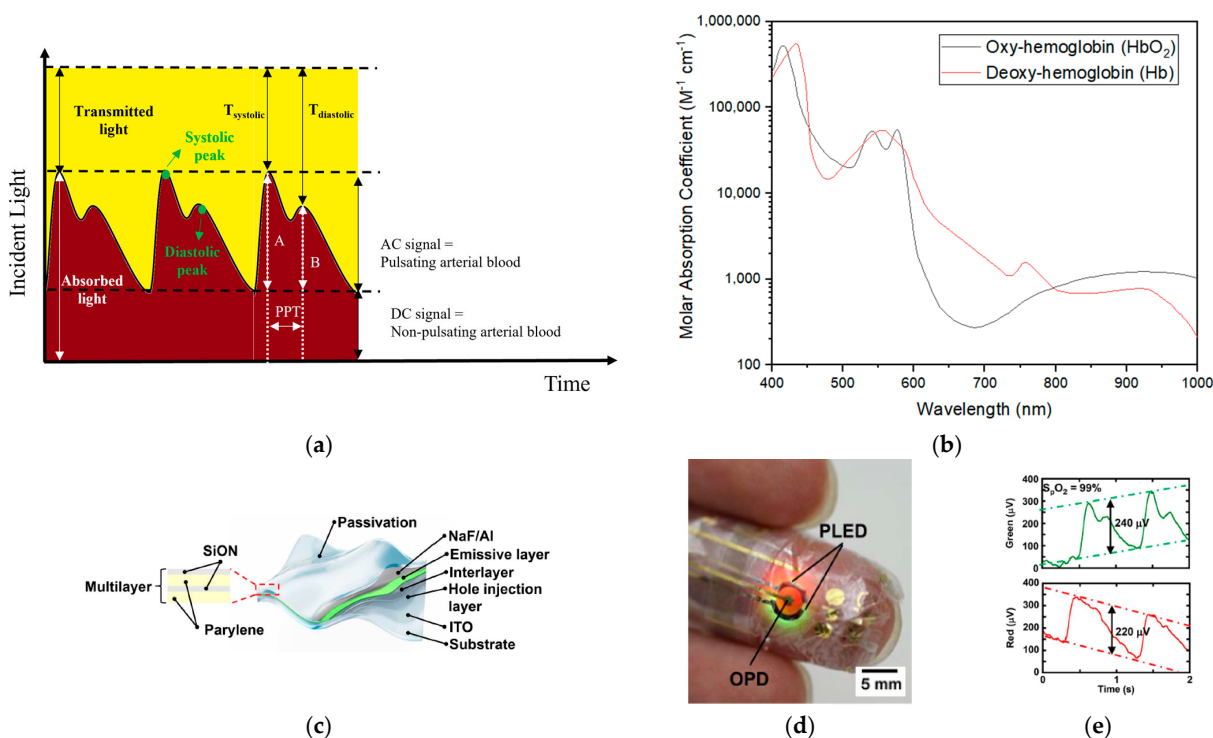


Figure 4. Images of photoelectrical signal measurement for skin-wearable devices. (a) The model for the pulse oximeter's light transmission path. (b) Molar extinction coefficient for hemoglobin in water. (c) Schematic of polymer LED with passivation layer composed by organic parylene layers and inorganic SiON layers. (d) The soft pulse oximeter taped on fingertip. (e) The output green (top) and red (bottom) PPG signals with 99% oxygenation of blood. (Reprinted/adapted from reference [59]).

PPG signals received at different wavelengths can be used to acquire SO_2 . In our body, hemoglobin plays an important role in carrying oxygen to our organs due to the limitation of oxygen dissolved in our blood (0.3 mL gaseous oxygen per 100 mL blood). The 100 mL blood contains up to 20.1 mL oxygen with the help of hemoglobin. One molecule of hemoglobin is only stable with four or zero oxygen molecules, and oxy-hemoglobin (HbO_2) and deoxy-hemoglobin (Hb) have different light absorptivity, especially with red ($\lambda = 660 \text{ nm}$) and near-infrared ($\lambda = 940 \text{ nm}$) light (Figure 4b) [145]. According to the Beer–Lambert Law, the absorption ratio of HbO_2 and Hb can be used to calculate SO_2 base on the light intensity attenuated by human tissue [58,146]; however, the result is limited by the tissue scattering (rather than a glass cuvette). In order to manufacture a commercial pulse oximeter, an empirical correction is required to overcome the limitation by analyzing the light absorption at two wavelengths from AC/DC volume [146,147].

Transmission and reflectance are two modes of accessing PPG and SO_2 . Transmission places the photodetector (PD) and light-emitting diodes (LEDs) on opposite sides of the tissue and detects the light signal that is transmitted through the vascular bed. In contrast, reflectance places the PD and LEDs on the same side of the body tissue and monitors the light signals that are reflected from the vascular bed [148]. Device placement in the transmission mode is limited because the device must be located on the body sites where light can be readily passed through. The most common sites for transmission are the fingertip and earlobe; however, these sites have limited blood perfusion and are susceptible to environmental extremes and daily activities [149]. Despite being under a static state reflectance presents less noise (due to less light scattering) [115], less fluctuation of the DC component (caused by a shorter light path) [13], and various possible placement sites throughout the body (even the wrists, forehead, ankle, and torso) [149,150]. Reflectance is also more susceptible to motion artifacts and pressure disturbances than transmission [149]. During physical activity under reflectance, the pressure interface skin device acting on the sensing probe causes deformation and the distortion of the arterial geometry. In addition, measurement sites and source–detector separation distance may also be factors affecting the result obtained from reflectance [115,151].

5.2. Photoelectric Signal for Skin-Wearable Devices

Although commercial devices are now able to minimize the size of components, the issue of skin–device attachment caused by rigid electronics still exists. Non-conformal contact leads to noise, especially during body movement; however, applying too much pressure to skin through the strips leads to torsion of the vessels and inaccuracy of the results. In contrast, the soft PPG has the potential to solve the current problem even when the body is in a dynamic state.

One approach is to use solution-processed electronics, which have better mechanical properties compared to current commercial devices. An organic optoelectronic sensor is one option for a skin-wearable pulse oximeter; however, organic LED materials are not stable in air and show low efficiencies [58]. Therefore, an all-organic pulse oximeter with green light ($\lambda = 532 \text{ nm}$) and red light ($\lambda = 626 \text{ nm}$) has been proposed due to the different light absorbability of HbO_2 and Hb at these wavelengths [58]. The result shows the ability of the device to detect PPG and SO_2 . Later, the green light ($\lambda = 517 \text{ nm}$) and red light ($\lambda = 609 \text{ nm}$) polymer LEDs were combined with an organic photodetector (poly(3-hexylthiophene) (P3HT): (6,6)-phenyl-C61-butyl acid methyl ester (PCBM)) to fabricate a soft pulse oximeter (Figure 4c–e) [59]. The passivation layers composed of organic parylene and inorganic SiON layers ensure that the LEDs can be operated in air up to 29 h. The soft and ultra-flexible pulse oximeter can be taped to a fingertip with clear pulsating curves for SO_2 calibration.

6. Mechanical Signal Measurement

6.1. Mechanical Signal Monitoring Mechanism

The pulse and blood pressure from arteries have been detected extensively on the skin surface over the radial and brachial artery for a long history, and this has been attributed to the artery's elasticity [152]. Although it is believed that the center aortic pulse wave is a better determination for clinical cardiovascular risk, direct measurement involves invasively inserting a catheter into the heart [153]. Currently, two non-invasive alternative methods have been applied to obtain aortic pressure by using mechanical pressure sensors in the field of arterial tonometry: the first is to record the pulse wave over the skin of the common carotid artery, which is considered to give a similar result as the carotid artery; and the second is to detect the pulse wave on the skin of the radial artery and apply the model to estimate the central pressure [154–156].

The schematic diagram of the obtained pulse wave is shown in Figure 5a [157], where systolic pressure (P1) is caused by left ventricular ejection, and renal reflection pressure (P2) and the iliac reflection pulse (P3) involve arterial blood propagating backward caused by the contraction of the left ventricle [158,159]. P2 represents the elasticity of the artery since the renal site is the junction of the aorta, where the diameter changes significantly. Therefore, the ratio between P2 and P1 is defined as the augmentation index (AI), which is the index of systemic arterial stiffness [157]. The stiffness of the arteries is related to the levels of collagen and elastin, which generally decrease with age and cause an increase in P2 [160,161]. Interestingly, in any age, women have a greater AI value than men, and yet women have lower cardiovascular risk than men [152,162]. Furthermore, the non-invasive pulse waves measured from the carotid and femoral arteries can be used to calculate pulse wave velocity (cfPWV). The cfPWV is measured by applanation to obtain arterial pulses at the carotid and femoral arteries, combined with the ECG reading as the time reference, and calculated using the subject's height as a distance [163]. Since the carotid–femoral pathway includes the aorta and its first branches, which are primarily responsible for pathophysiological arterial stiffness, cfPWV is considered a “gold standard” for arterial stiffness [164–166]. The stiffer arteries present an increase in the cfPWV value with a cut-off value of 10 m/s [167,168]. Non-invasive cfPWV detection without physiological impact is of great significance for the recovery of patients after complex surgery (such as angiogenesis); however, current clinical detections apply planar and rigid formats, and are attached on skin by mechanical fixtures, such as straps and tapes [68]. Continuous monitoring with such devices is difficult, especially after patients are discharged from the hospital.

Mechanical pressure sensors can also help with the assessment of skin diseases. The mechanical properties of human skin are mainly derived from the contributions of connective tissue, the dermis, subcutaneous tissue, and the epidermis [169]. The first works about the mechanical properties of human skin began with Dupuytren in 1834 and Langer in 1861, who mainly studied the anisotropy of the natural stress and strain fields of skin [170]. Changes in the mechanical properties of human skin reflect tissue modifications, which are caused by sex [170], aging [171], skin lesions [172], and the hydration of cosmetics [172]. Traditional measurements (such as suction, indentation, traction, torsion, and wave propagation) provide the results that are affected by external variables, such as pressure applied to skin, skin thickness, and detection area [36,170,173]. By contrast, soft skin-wearable pressure sensors can not only address these issues through conformal skin contact but also enable long-term monitoring in patients' daily lives. Furthermore, recent studies have proposed skin-wearable ultrasound devices based on mechanical (acoustic) signal detection [32,71,174].

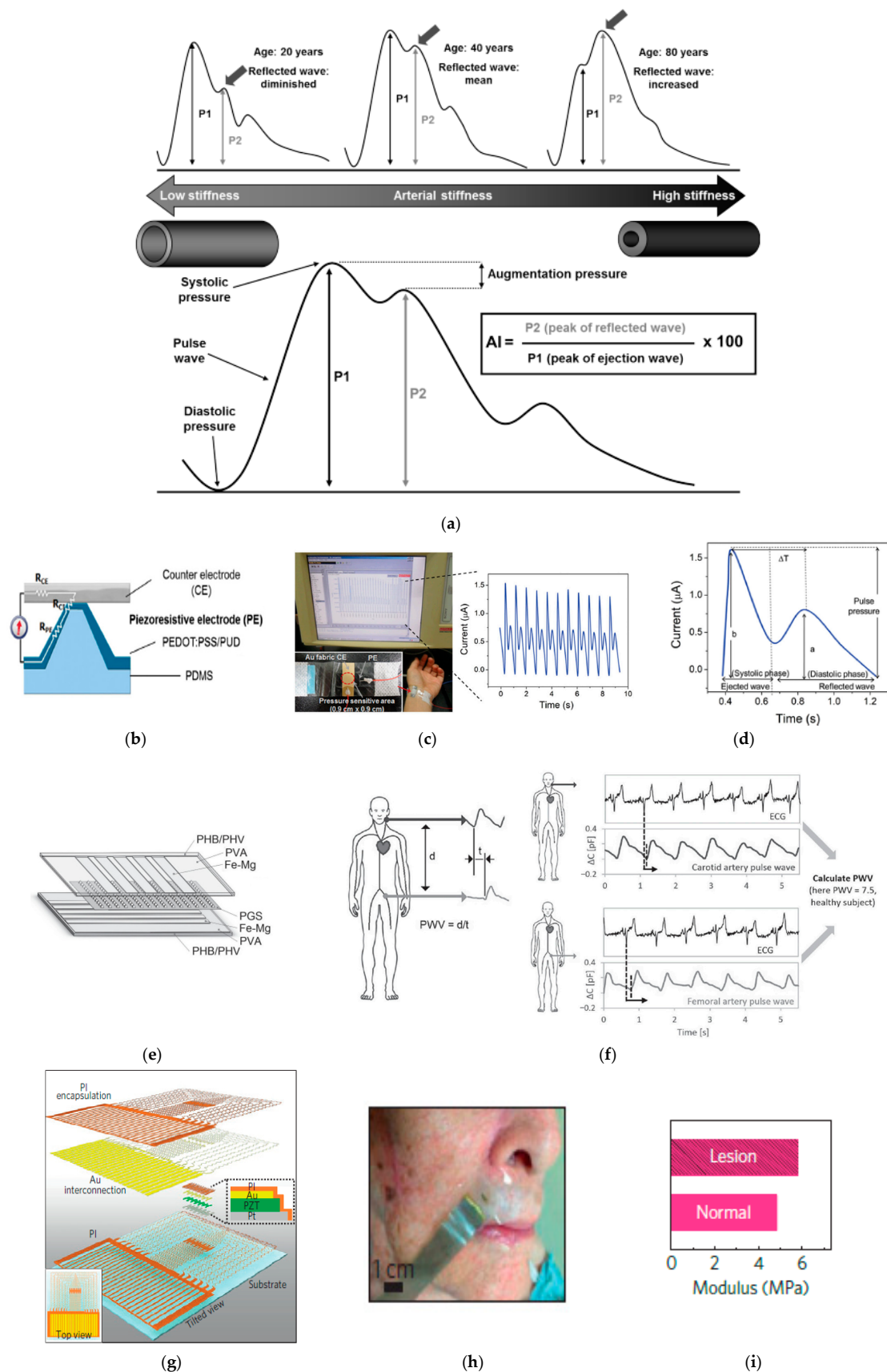


Figure 5. Images of skin-wearable mechanical pressure sensors to detect sweat analytes. (a) Schematic of the variables that determine the Augmentation Index (AI). (b) Circuit mode of piezoresistive sensor fabricated in PDMS pyramid structure and coated with PEDOT:PSS/PUD thin film. (c) The device

is placed on the subject's wrist (left) and the detected signal (right). (d) The detected important features of the pulse wave for health monitoring. (e) Schematic of the biodegradable and flexible capacitive pressure sensor. (f) Combined with ECG measurement, blood pulse waves detected by the capacitive pressure sensor can be used to measure pulse wave velocity. (g) Schematic of the piezoelectric device for skin biomechanics. (h) The conformal device mounted on the near nose region of the subject and (i) the collected data under actuation voltage and frequency of 5 V and 1 Hz, respectively. (Reprinted/adapted from reference [157]; Reprinted/adapted with permission from reference [60], Copyright 2014, Advanced Materials; Reprinted/adapted with permission from reference [64], Copyright 2015, Advanced Materials; Reprinted/adapted with permission from reference [69], Copyright 2015, Nature Materials).

6.2. Mechanical Signal for Skin-Wearable Devices

Currently, the proposed skin-wearable pressure sensors mainly focus on three mechanisms: piezoresistivity, capacitance, and piezoelectricity (Table 3).

Table 3. Summary of pressure sensors and their properties.

Pressure Sensor Classification	Sensitivity	Response Time	Stretchability	Operating Voltage	Healthcare Monitoring	Refs
Piezoresistivity	4.88 kPa ⁻¹ (0.37 < ρ < 5.9 kPa)	0.2 s	50%	0.2 v	Wrist blood wave	[60]
	25.1 kPa ⁻¹ (ρ < 2.6 kPa)	80–120 ms	N/A	N/A	physiological signals, voice, and motion activities	[61]
	0.0021 kPa ⁻¹ (ρ < 2.3 kPa); 0.0044 kPa ⁻¹ – 0.0109 kPa ⁻¹ (2.3 kPa < ρ < 80 kPa)	22 ms	80%	N/A	Early-stage Parkinson's disease (tremor of 4–6 Hz)	[62]
	0.0834 kPa ⁻¹ – 0.0835 kPa ⁻¹ (ρ < 0.8 MPa)	90 ms	Stretching > 200% strain without failure	30 mV	Cardiology	[63]
Capacitance	0.76 ± 0.14 kPa ⁻¹ (ρ < 2 kPa); 0.11 ± 0.07 kPa ⁻¹ (2 < ρ < 10 kPa)	millisecond	Bending radii down to 27 mm, sensitivity remains 80%	N/A	Cardiology, arterial stiffness	[64]
	0.51 kPa ⁻¹	0.15 s	>40 compression (10,000 cycles)	N/A	Cardiology, early-stage Parkinson's detection, muscle movement, vocalization waves	[65]
	2254 kHz mmHg ⁻¹	90 ms	N/A	Nearfield electromagnetic coupling	Cardiology, intracranial pressure	[66]

Table 3. Cont.

Pressure Sensor Classification	Sensitivity	Response Time	Stretchability	Operating Voltage	Healthcare Monitoring	Refs
Piezoelectricity	10 kPa	~0.1 s	N/A	3 V	Cardiology, arterial stiffness	[67]
	3.95 V N ⁻¹	39 ms (static state)/27 ms (excited state)	Bending angle up to 90°	N/A	Cardiology, voice recognition	[70]
	~0.005 Pa	~0.1 ms	stretching ~30% with effective modulus of ~60 kPa	1–3 V	Cardiology, arterial stiffness	[68]
	(30 < ρ < 1800 kPa)	N/A	Stretching 30% (failure)	2–5 V	Dermatology	[69]

The transduction behavior of piezoresistivity, which transfers a mechanical displacement into an impedance change, is suitable for soft electronics due to its sensitivity to structure deformation caused by applied pressure [175]. Piezoresistive sensing has a simple read-out mechanism [176], and a fast response to structural deformation [177]. Adjusting the shape structure between the two sheets is key to improving the sensitivity of the piezoresistive sensor. However, piezoresistive sensors have limitations, such as temperature dependence [178], a powering supply requirement [179], and low sensitivity, especially with ultra-low pressure being applied [180]. Poly(dimethylsiloxane) (PDMS) was patterned into a micronized pyramid structure and coated with (poly(3,4-ethylenedioxythiophene–poly(styrenesulfonate) (PEDOT:PSS) and an aqueous polyurethane dispersion (PUD) composite polymer for pulse wave sensing (Figure 5b–d) [60]. The stretchable device with a sensitivity of 4.88 kPa⁻¹ (0.37 < ρ < 5.9 kPa) can be attached on the wrist and can measure a pulse pressure of 170 Pa (or 1.3 mmHg) with the low operation voltage of 0.2 V. Another structure is the epidermis-inspired microstructure, which consists of Merkel disks that resemble abrasive paper topography [61]. In one study, PDMS was patterned on abrasive paper for a spinosum microstructure and coated with graphene oxide (GO). The device can detect physiological signals, such as pulse waves from the wrist, respiration states from the chest, and motion activities from the feet. The sensor was able to be attached to a volunteer's arm for 2 days without discomfort or allergic reaction. Furthermore, a bioinspired beetles' wing-locking structure has been used for piezoresistivity [62]. The supramolecular assembly of graphene oxide (GO) was first applied onto the hydrophobic polyurethane (PU) sponge and then obtained the conductive polyaniline nanohair (PANIh) arrays by in situ reduction. The device can withstand up to 80% deformation with a high sensitivity of 0.0021 kPa⁻¹ (ρ < 2.3 kPa). The device can also detect a low-frequency of 4–6 Hz, which provides the possibility of predicting early-stage Parkinson's disease with imitated static tremors. Eutectic gallium–indium (EGaIn), the liquid metal alloys, can also be used to build a wearable piezoresistivity sensor by embedding it into microchannels made of PDMS [63]. The conductive material can be substituted by EGaIn due to its low toxicity and high electrical conductivity. In the study, EGaIn was formed into an equivalent Wheatstone bridge circuit. The device presents a high sensitivity of 0.0835 kPa⁻¹ and 0.0834 kPa⁻¹ for loading and unloading, respectively. The PDMS wristband of a 1.8 mm diameter pressure sensor was attached to the subjects to measure a clear output dynamic pulse wave.

Capacitive sensors measure elastic deformation by detecting the changes in electrical capacitance. The capacitance (C) of a parallel plate capacitor is given as:

$$C = \epsilon_0 \epsilon_r A/d \quad (3)$$

where ϵ_0 is the free space permittivity as the constant, ϵ_r is the relative permittivity, A is the area, and d is the distance between electrodes [181]. The simplicity of the governing equation simplifies the device design and analysis [182]. Although capacitive sensors have high sensitivity, low power consumption, and resistance to temperature variation, they are susceptible to interference from external sources [181,183]. A pyramid structure has also been used for capacitive sensing in healthcare monitoring. The wearable electronic uses biocompatible materials that make it biodegradable. It is composed of Poly (glycerol sebacate) (PGS) to form the pyramid structure, polyhydroxybutyrate/polyhydroxyvalerate (PHB/PHV) as the substrate, magnesium (Mg) as the electrodes, and iron (Fe) as an adhesion layer for Mg (Figure 5e,f) [64]. The Young's modulus of PGS is within range of 0.05–2 Mpa, which ensures that it can take the place of PDMS (Young's modulus ~ 1 Mpa). The device presents the pressure sensitivity of 0.76 kPa^{-1} ($\rho < 2 \text{ kPa}$). The cfPWV was measured with the value of 7.5 m/s when applied the soft device onto the subject and used the ECG result as a time reference. MXene (Ti₃C₂T_x)/poly (vinylidene fluoride-trifluoroethylene) (PVDF-TrFE) composite nanofibrous scaffolds have been used as a dielectric layer between poly-(3,4-ethylenedioxythiophene) polystyrene sulfonate /polydimethylsiloxane (PEDOT:PSS) electrode layers to form a capacitive pressure sensor for pulse wave detection [65]. The sensitivity of the device can reach 0.51 kPa^{-1} with a minimum detection limit of 1.5 Pa. The device can be used to detect multiple pressure changes on the skin, such as a pressure pulse wave on the wrist, those caused by the initial stage Parkinson's disease, muscle contraction and expansion, muscle vibrations during eye twitching, and voice recognition. Another alternative to PDMS is styrene-butadiene-styrene (SBS) due to low dielectric loss in the high frequency range [184]. In the study, the pyramid elastomer was patterned onto the spatial copper design, which was coated on polyimide [66]. The sensor achieved wireless operation by near-field electromagnetic coupling between the resonant sensor and an external antenna. The design can capture the pulse wave with a pressure resolution of 0.3 mmHg and a time resolution of 90 ms and can even measure intracranial pressure when implanted in mice.

Piezoelectricity occurs in certain materials (such as crystal, ceramics, and piezoelectric or electroactive films) that accumulate electrical charge in response to an applied mechanical force, changing the distance between dipoles of the material [182,185]. The ability of a material to convert mechanical force to an electrical charge can be described as d_{33} , the piezoelectric coefficient:

$$d_{33} = \sigma / \rho \quad (4)$$

where σ is the charge density and ρ is the applied force [186]. Although piezoelectric sensors have high sensitivity, a rapid response, and the potential for self-power [187,188], they exhibit thermal drift over time [189]. Ferroelectric materials have been widely used in piezoelectric sensors. The researchers used a printed ferroelectric polymer, poly(vinylidene fluoride-co-trifluoro ethylene) [P(VDF-TrFE)]-based pressure detector to fabricate a flexible device with PEDOT:PSS electrodes and a layer of poly(ethylene naphthalate) (PEN) substrate [67]. The device also consists of organic thin-film transistors (OTFTs) in a Darlington connection to amplify the signal by a gain factor of 10. The design ensures a sensitivity below 10 kPa and a fast response time of ~ 0.1 s. It can monitor pulse waves and the cfPWV (9 m/s) of the subject. A muscle structure-inspired piezoelectric sensor has been made by dispersing polydopamine (PDA) into barium titanate/polyvinylidene fluoride (BTO/PVDF) nanofibers to form interfacial bonds through an active surface functional group [70]. The fabricated nanofiber layer was bilaterally laminated with aluminum foils and used electrodes and flexible PET as substrates to realize a wearable device with a sensitivity of 3.95 V N^{-1} . Lead zirconate titanate (PZT), the electric/piezoelectric material, has been arranged in an array for pulse wave and cfPWV sensing [68]. The detected signal can be amplified by a silicone nanomembranes (SiMNs) n-channel metal semiconductor field effect transistor (n-MOSFETs). The conductive metal serpentine traces and the silicone substrate ensure the device can be stretched up to $\sim 30\%$ while maintaining the sensitivity of $\sim 0.005 \text{ Pa}$. Furthermore, PZT-based nanoribbons were constructed as ultrathin stretchable

networks for in vivo viscoelasticity measurements of epidermis lesions (Figure 5g–i) [69]. Due to the water-soluble polyvinyl alcohol (PVA) and the filamentous serpentine traces on the silicone substrate, the device can be attached to the skin by van der Waals forces alone with adequate stretchability. The polyimide encapsulated capacitor components were fabricated by a layer of piezoelectric PZT interposed between a Ti/PT bottom layer and a Cr/Au top electrode. The conformal device consists of seven actuators and six sensors for detection. Sensing involves outputting sinusoidal voltage changes through a selected actuator to induce mechanical motions in the PZT, surrounding elastomer, and the underlying epidermis. The mechanical coupling of the skin and elastomer causes the deformation of adjacent PZT. The results obtained from 30 patient volunteers using the device showed that the moduli of skin lesions on the breast and legs were lower than that of healthy skin, while the moduli of the nose and forehead area were higher than that of healthy skin.

6.3. Acoustic Signals Measurement

An acoustic wave is a mechanical wave that propagates along or through a medium via interactions between particles. The human ear perceives an acoustic frequency from 0.02 to 20 kHz. Diagnostic ultrasound scanners operate in the frequency range of 2 to 18 MHz, which is much higher than the human ear perceives [190]. Higher frequencies have correspondingly shorter acoustic wavelengths, which produce higher-resolution images; however, shorter wavelengths prevent penetration into deeper tissues. Therefore, higher frequency ultrasound (20 to 50 MHz) benefits from high-resolution images with low tissue penetration depth and is currently widely applied in dermatological diagnosis and treatment [191].

An ultrasound pulse is produced by passing an electrical current through a piezoelectrical crystal element. The element converts the electrical energy into a mechanical ultrasound wave. The frequency of the wave is determined by the thickness of the crystal. The thicker crystal element produces lower frequencies while the thinner crystal element produces higher frequencies. When the wave propagates through materials of different densities in the body, a frequency shift occurs due to the different mechanical properties of the materials. The reflected echo returns to the transducer, which converts the shifted ultrasound wave into an electrical signal. Diagnostic sonography is an ultrasound-based medical imaging diagnostic technique that enables the visualization of muscles and internal organs, offering visuals of their size, structure, and potential pathological lesions. The continuous monitoring of deeper tissues and internal organs has clinical value; however, long-term monitoring is limited by unstable coupling to tissue surfaces due to the bulkiness and rigidity of the existing non-invasive ultrasound equipment [192]. In addition, since the ultrasonic wave cannot transmit in air, an ultrasonic coupling must be used and pressure must be applied to reduce impedance and facilitate the transmission of sound energy between the transducer and the test sites. Such requirements have resulted in ultrasonography being available on limited body sites, since pressure over the carotid artery, jugular vein, and vagus nerve could cause suffocation [32]. Furthermore, sonographers also suffer from work-related musculoskeletal disorders due to the prolonged use of the transducer, repetitive motions, and static work postures [193,194].

One approach to long-term ultrasonic monitoring is to apply rigid ultrasound probes on a bioadhesive hydrogel elastomer coupling to form a bioadhesive ultrasound (BAUS) device (Figure 6a–c) [32]. The BAUS coupling consists of a hydrogel formed by chitosan-polyacrylamide interpenetrating polymer networks (10 wt%) and water (90 wt%). The hydrogel is encapsulated by an elastomer membrane of polyurethane. The hydrogel-elastomer hybrid is further coated by a thin bioadhesive layer, which can form physical bonds and electrostatic interactions with the skin. The BAUS probe consists of an array of piezoelectric elements, which enable a high density of elements and high-resolution images. With a center frequency of 3, 7, and 10 MHz, the electrical impedance of the probes at the

center frequencies are 49, 36, and 43 ohms, respectively. The BAUS device can provide images of the blood vessels, stomach, lungs, diaphragm, and heart for over 48 h.

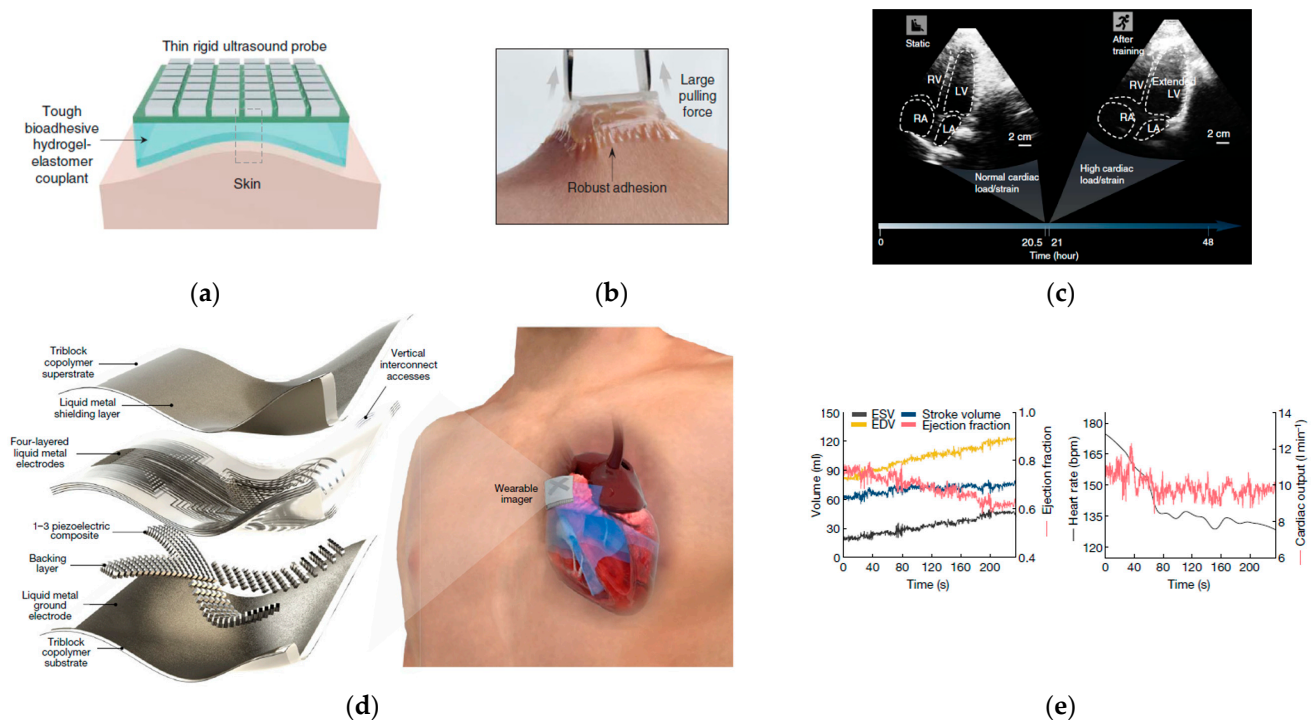


Figure 6. Images of skin-wearable acoustic signals. (a) Schematic of BAUS device, which consists of a thin and rigid ultrasound probe and can be attached to skin via a hydrogel–elastomer hybrid. (b) Skin-attached BAUS device under high pulling forces. (c) The BAUS imaging shows the dynamics of the four chambers of the heart. (d) Schematic diagram of the wearable cardiac ultrasound imager (left) and its working principle (right). (e) The extracted information of stroke volume, ejection fraction (left), and cardiac output (right) from consecutive images by a deep learning model. (Reprinted/adapted with permission from reference [32], Copyright 2022, Science; Reprinted/adapted from reference [71]).

The second approach is to fabricate a stretchable ultrasound probe to be worn on the skin. The stretchable ultrasound device can be built with metal traces, using electrodes and piezoelectric 1–3 composite as transducer materials [174]. In addition, the wearable ultrasound imager with high stretchability of up to approximately 110% has also been built to detect the critical cardiac features (Figure 6d–e) [71]. The device was built by utilizing liquid metal as the electrodes, triblock copolymer (styrene–ethylene–butylene–styrene (SEBS)) as the substrate, and 1–3 piezoelectric composite (PZT-5H) as the ultrasound transducer. The center resonant frequency of the device is 3 MHz and the penetration is greater than 16 cm. The device can also detect cardiac activities before, during, and after exercise. A deep learning model was applied to extract information, such as stroke volume, cardiac output, and ejection fraction, from sequential images.

7. Electrochemical Signal Measurement

7.1. Electrochemical Signal Monitoring Mechanism

Human sweat is a biofluid that contains electrolytes and metabolic wastes that can reflect the condition of plasma [195]. It is produced by the secretory coils of eccrine glands and delivered to the surface of skin through dermal ducts (Figure 7a) [196]. The most accessible analytes in our sweat and the methods to detect them are shown in Table 4. The life-essential analytes depend on each other while having their own balance [197–199]. Concentrations beyond the range may cause certain diseases, which can be diagnosed early and treated via sweat detection. Among the analytes, the most abundant ion species are

sodium (Na) and chloride (Cl), for which levels are elevated with an increase in sweat rate [199]. A concentration of Cl^- in excess of 60 mM indicates cystic fibrosis [200,201], an inherited chronic disease affecting the lungs and digestive system [202]. The depletion of ionized potassium (K^+) is associated with heat-illness [203]. Loss of ionized calcium (Ca^{2+}) in sweat accounts for up to 30% of daily body losses [204]. Ca^{2+} levels effect the structure of many organs and body systems. Low levels of Ca^{2+} can lead to disease, such as cirrhosis and renal failure [205,206], while high levels of Ca^{2+} can lead to hyperparathyroidism [207]. High ammonia levels can be used as markers of hepatic disorders, such as hepatitis or cirrhosis [208]. It is noticeable that ammonia levels in sweat are higher than in blood due to the high pH of sweat [209]. Changes in skin pH value can result in skin disorders such as dermatitis, atopic dermatitis, ichthyosis, acne vulgaris, and fungal infections [210]. Sweat lactate is a hallmark of pressure ischemia, manifested by insufficient oxidative metabolism and impaired tissue vitality [211]. So far, there is no evidence that shows that sweat lactate is related to blood lactate or skin pH value [212]. Similarly, a precise relationship between skin glucose and blood glucose requires further evidence of correlations, since at least three parts of skin can produce glucose (stratum corneum, outward migration of interstitial fluid, and sweat) [213]. Heavy metals, such as copper (Cu) and zinc (Zn), are also essential elements, but in limited amounts in the body [214]. Excessive Cu levels lead to Wilson diseases [215], while insufficient Zn levels affect the immune system by impacting wound healing and even DNA synthesis [214]. In addition to essential analytes, sweat secret toxic metals, such as cadmium (Cd), mercury (Hg), and lead (Pb), accumulate in our bodies for a lifetime without producing physiological benefits [216]. These toxic metals can enter our bodies in daily life. For example, Cd and Hg accumulate in seafoods and tobacco, and Cd, Hg, and Pb are all found in products such as electronics, batteries, and alloys [217].

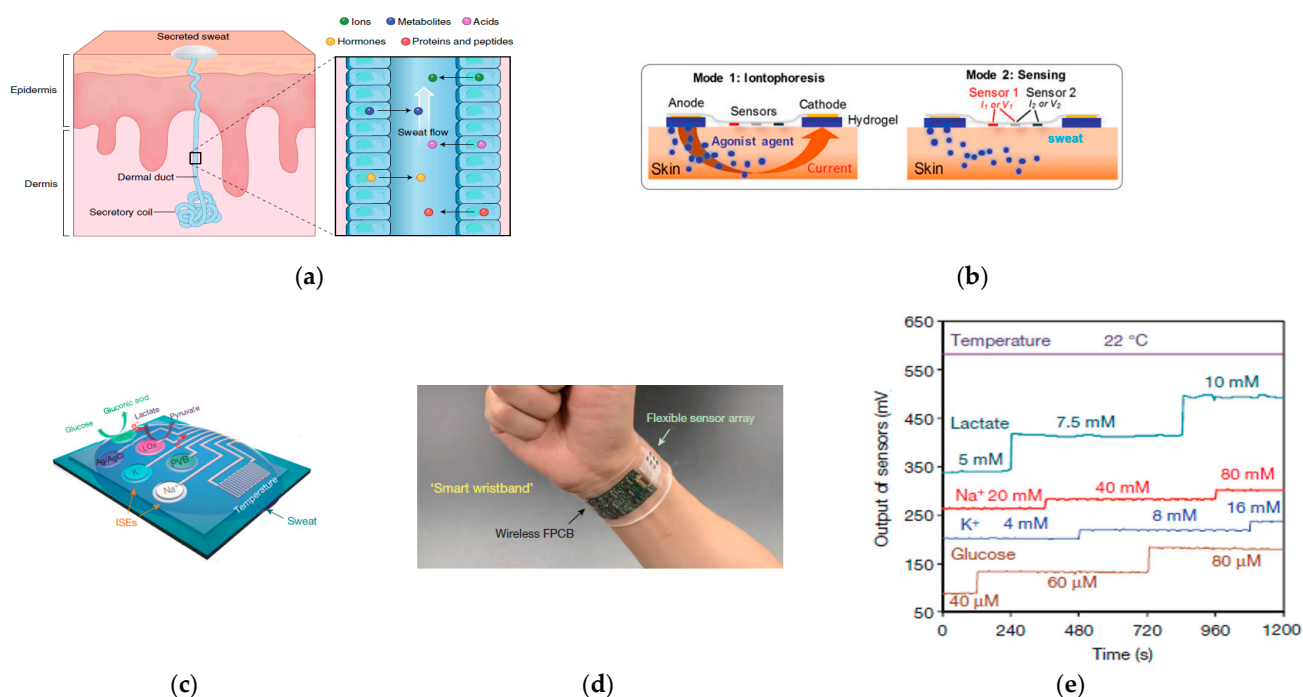


Figure 7. Images of skin-wearable electrochemical devices to detect sweat analytes. (a) Schematic of sweat gland and bioelectrolytes. (b) Illustrations of iontophoresis method for sweat sensing. (c) Schematic of the multisensing elements for sweat analytes. (d) Image of the device worn on subject's wrist. (e) The device outputs multiple sense responses simultaneously. (Reprinted/adapted with permission from reference [196], Copyright 2016, Nature; Reprinted/adapted from reference [200]; Reprinted/adapted with permission from reference [221], Copyright 2016, Nature).

Table 4. Analytes in sweat and their on-body detection methods.

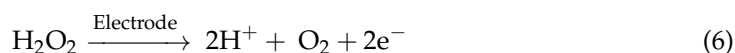
Analyte	Concentration in Sweat [196]	Method	Substrate	Recognition Element	Refs	
Sodium	10–100 mM	Potentiometry	Temporary tattoo	Sodium ionophore	[218]	
			Adhesive Tape	Sodium ionophore	[219]	
			PMMA	Sodium ionophore	[220]	
			PET	Sodium ionophore	[200,221]	
Chloride	10–100 mM		Polyester	Ag/AgCl	[201]	
			PET	Ag/AgCl	[200]	
Potassium	1–18.5 mM		PET	Potassium ionophore	[221]	
Calcium	0.41–12.4 mM		PET	Calcium ionophore	[222]	
Ammonia	0.1–1 mM		Temporary tattoo	Nonactin ionophore	[223]	
Heavy metal	Pb	<100 $\mu\text{g L}^{-1}$	Square-wave stripping voltammetry	PET	Bismuth, gold	[224]
	Cd	<100 $\mu\text{g L}^{-1}$		PET	Bismuth	[224]
	Hg	<100 $\mu\text{g L}^{-1}$		PET	Gold	[224]
	Cu	100–1000 $\mu\text{g L}^{-1}$		PET	Gold	[224]
	Zn	100–1560 $\mu\text{g L}^{-1}$		PET	Bismuth	[224]
pH	3–8 (4–6.8)	Potentiometry	Temporary tattoo	Bismuth	[225]	
			PET	Hydrogen ionophore	[222]	
		Colorimetry	PMMA	Poly(aniline)	[226]	
			PMMA	Poly(aniline)	[220]	
Thermal properties	36.5–37.5 °C		PMMA	Bromophenol green (BCG), bromophenol purple (BCP)	[227]	
			PDMS	bromophenol purple (BCP)	[228]	
Lactate	5–20 nM	Chronoamperometry	PET	Thermochromic liquid crystals	[229]	
			Temporary tattoo	Lactate oxidase	[230]	
			Parylene	Lactate oxidase	[231]	
			PMMA	Lactate oxidase	[220]	
Glucose	10–200 μM		PET	Lactate oxidase	[221]	
			PET	Glucose oxidase	[200,221]	

7.2. Electrochemical Signal for Skin-Wearable Devices

Sweat is detected by a rigid collector that is attached to skin by applied pressure. The device absorbs sweat via capillary forces and tests the sweat via an off-body method. Sensitivity and the reliability of results are limited due to evaporation and chemical degradation during the process [209]. Therefore, an on-body device capable of continuous acquisition and sensing at the point of generation is demanded to overcome the limitations.

One approach to on-body sensing is colorimetric detection, which has been used to detect skin thermal properties [229], pH value, and the levels of glucose, lactate, and chloride [228]. One study formed soft serpentine microchannels (3 mm in diameter) using PDMS to absorb sweat by capillary forces, and analyzed the relationship between color change and concentrations on site [228]. The device can measure total sweat loss over time and use ultraviolet (UV)-visible spectroscopy to quantify analyte concentration. It contains near field communication (NFC) electronics that enable wireless communication with smart devices. In addition, colorimetric exposure can be used to detect the thermal properties of skin using thermochromic liquid crystals [229].

Electrochemical detection provides an alternative approach due to the high sensitivity and rapid response of measuring currents or potentials on-site [209]. It includes potentiometry, chronoamperometry, and voltammetry. By applying potentiometry, iontophoretic electrode-induced sweat can be analyzed on-site immediately by highly sensitive sensors located on the same substrate as the relevant sensing targets (Figure 7b) [200]. Iontophoresis of sweat sensing is applied for transdermal drug delivery systems [232,233], which help ameliorate the symptoms of pain relief [234], chronic edema [235], and rheumatic condition [236]. Since the concentration of the target analyte is based on the potential difference between the sensing electrode and the reference electrodes, this method can only be used to detect charged species, such as Na^+ , Cl^- , K^+ , Ca^{2+} , and H^+ (pH) [209]. Glucose, lactate, and ethanol can be detected by chronoamperometry, which relies on the specific enzymes to oxidize and generate a current proportional to their concentration [209]. Here is an example of the process for lactate [237]:



In practice, one device can contain one or more sweat analysis methods. For example, one study integrated sensing elements on a PET substrate that simultaneously detected glucose, lactate, Na^+ , and K^+ via chronoamperometry and potentiometry (Figure 7c–e) [221]. The device also contained metallic traces to compensate for surrounding temperature. The circuit components, such as amplifiers, filters, and wireless transmission, are consolidated into a flexible printed circuit board (FPCB), and the device can be worn on the subject's wrist. Furthermore, trace metals (Cu^{2+} , Zn^{2+} , Cd^{2+} , Pb^{2+} , Hg^+) can be detected by square wave anodic stripping voltammetry (SWASV), which uses gold and bismuth as electrodes. Researchers fabricated a soft sensing array on PET substrate with gold (Au) and bismuth (Bi) as the working electrodes (WE), silver as the reference electrode (RE), and Au as the counter electrode (CE) [224]. The integrated sensing part can be bent with curvature radii of 3.2 mm and can be attached to skin with a wristband. The result shows that an Au electrode is suitable for Pb, Cu, and Hg, while a Bi electrode is suitable for Zn, Cd, and Pb.

Among secretions from skin other than sweat, the volatile organic compounds (VOCs) released from skin are also non-invasively detectable and can provide important clinical information [238]. Similarly to sweat, skin VOCs are a mixture of compounds that are generated from metabolic processes. It is known that breath is the largest contributor of VOCs in humans [239]. As the secondary source of VOCs, skin-emitted VOCs have a correlation with breath [240]. The VOCs from breath have been well studied, as the signals can be sensed by optical sensors, colorimetric sensors, surface acoustic wave sensors, piezoelectric sensors, metal oxide sensors, silicon nanowire sensors, and monolayer-coated

metal nanoparticle sensors [241], while research from soft/stretchable skin-wearable VOC detection devices is limited. Moreover, VOCs testing cannot be applied for early diagnosis, and must be combined with other strategies to increase diagnostic accuracy [241]. Regardless, VOCs detection can be used as one of the important supplementary sources of health monitoring.

8. Future Challenges and Opportunities

Skin-wearable sensors offer the opportunity to read health information non-invasively through human skin. Soft skin-electronic contacts reduce impedance and improve signal-to-noise ratio. Tests of the reviewed sensors demonstrate the feasibility of their applications. Future devices can be improved from the following aspects.

Despite the fact that the lifespan of skin-wearable devices is constrained to 2 weeks, due to the exfoliation of the stratum corneum [8], few of the studies reviewed here achieved realistic monitoring up to 2 weeks (Table 5). In fact, most studies on conformal contact have not been tested for hours, and only few studies have demonstrated the two-week adhesion length. Wired power and communication are the main reasons for limiting long-term monitoring. Several studies have proposed solutions for wireless communication, such as stretchable solar cells [34], triboelectric mechanisms [242], bioelectrocatalytic reactions [243–245], soft solid batteries and capacitors for on-body power generation [246,247], and near field communication (NFC) [66,229]. Therefore, combining such technologies with skin-wearable sensors could potentially make products more valuable. Accelerated life testing can further examine the effective duration of a device's lifespan.

Self-learning techniques can be further implemented on skin-wearable devices for immediate diagnosis and abnormality alerts. Current analyses of electrophysical signals are mainly conducted through visual assessment, which is considered time-consuming and as low-yield work. However, sudden illness, such as seizures, requires continuous signal monitoring and data reviewing for hours or even days [102]. Additionally, inconsistent conclusions will be drawn by the inspectors' level of expertise. Combining convolutional neural networks similar to a multilayer perceptron with deep learning to automatically recognize and classify given information for the analysis of ECG, EEG, and EMG is urgently required these days [102,144,248]. This point-of-care detection and diagnostic technology has the potential to take skin-wearable sensors to a new era. Initiative actuators embedding provides the opportunity for disease treatment and rehabilitation. Current skin-wearable devices mainly focus on the passive monitoring of health messages. Early treatment is one of the improvements that broadens the application range of existing designs. So far, actuators have been integrated into wearable devices for EMG [37,50]. Through the self-learning process of practice and simulation, patients are able to drive prosthesis readily by inputting electric power.

Beyond health-related monitoring and quick diagnoses, safety assessments will drive more interest for wearable sensors/devices since they can provide strong safety-related crisis management systems for human being. The non-biocompatibility of skin-attached sensors can lead to many complications, including cell cytotoxicity, skin irritation, skin sensitization, and skin chronic inflammation, and can also lead to commercial product recalls due to reported dermatitis. The U.S. Food and Drug Administration (FDA) and the International Organization for Standardization (ISO) require that skin-contact devices be evaluated for cytotoxicity, sensitization, and irritation [249–251]. To validate skin-wearable devices for public use, skin–material compatibility cannot be ignored.

Table 5. Summary of useful adhesion duration.

Substrate Material	Device Thickness	Placement Site (Signal)	Exercise/Motion	Adhesion Length	On-Skin Measurement Duration	Ref
00-30 Ecoflex	37 μm	Skin (temperature), forehead (EEG), chest (ECG), leg (EMG)	Walking, skin stretching	N/A	6 h	[36]
Ecoflex 00-30	N/A	Wrist (blood pulse)	N/A	N/A	14 s	[68]
Ecoflex 00-30	20 μm	Skin (dermatology)	N/A	N/A	N/A	[69]
Ecoflex 00-30/ Bluestar 4642	0.9 mm	Arm (EMG), scalp (EEG)	Exercise, sleeping and showering, skin stretching	Consistent over several days	30 s	[50]
Ecoflex	$\sim 140 \mu\text{m}$	Forearm, fingertip (blood flow)	Device compressing	N/A	30 min	[56]
PDMS	2 mm	Arm (ECG), scalp (EEG)	Swimming	N/A	70 s	[5]
PDMS	20 μm	Arm (ECG)	Wrist curl, squat, writing	N/A	40 s	[30]
PDMS	300 μm	Wrist (blood pulse)	N/A	N/A	10 s	[60]
PDMS	20 μm	Wrist (blood pulse), foot (pressure)	Walking, running, jumping	N/A	30 s	[61]
PDMS	N/A	Wrist (blood pulse)	Bike riding	N/A	1400 s	[63]
PDMS	700 μm	Skin (sweat)	Bike riding	N/A	1–6 h (one-time usage)	[228]
Adhesive PDMS	120 μm	Chest (ECG)	N/A	N/A	20 s	[49]
Adhesive Bluestar Silicones	2 mm	Chest (ECG), arm (EMG), neck (EEG)	N/A	N/A	20 s	[51]
SBS	0.1 mm	Wrist (blood pulse)	N/A	N/A	60 s	[66]
Silicone elastomer	3 μm	Ear (EEG)	Washing in soap water	2 weeks	3.5 min	[48]
PHB/PHV	2.4 mm	Wrist (blood pulse, PWV)	N/A	N/A	15 s	[64]
Silicone elastomer/PVA	$\sim 50 \mu\text{m}$	Palm (temperature)	Device compressing	N/A	3 h	[4]
PVA	$\sim 30 \mu\text{m}$	Bicep and tricep, lower back (EEG)	Skin stretching	2 weeks	30 s	[37]
PET	$\sim 30 \mu\text{m}$	Chest (ECG, temperature)	Running	30 h	2000 s	[46]
PET	N/A	Skin (sweat)	Bike riding	N/A	7000 s	[221]
PEN	50 μm	Wrist (blood pulse, PWV)	N/A	N/A	3 s	[67]
Parylene	30 μm	Fingertip (PPG/SO ₂)	N/A	5 days	3 s	[59]
Polyurethane sponge	N/A	Wrist (blood pulse), static tremor (Parkinson's disease diagnosis)	N/A	N/A	80 s	[62]

In summary, skin-wearable sensors are interdisciplinary devices that involve medicine, materials, machinery, electrical hardware, software, etc. The development of skin-wearable sensors depends on the development of each discipline. Skin-wearable electronics can detect vital health information and have the potential to overcome the limitations of current rigid devices. Soft, conformal skin-electronic contacts provide opportunities for long-term continuous health monitoring with results comparable to commercial methods. In the foreseeable future, skin-wearable electronic devices should become a mainstream medical monitoring method because of improvements such as a wireless power supply and communication, self-learning diagnostic techniques, early treatment, and overall safety assessment. Through the combination of different technologies, wearable electronics can not only be used to monitor and diagnose diseases but also help disease treatment and rehabilitation.

Funding: This research received no external funding.

Institutional Review Board Statement: Not applicable.

Informed Consent Statement: Not applicable.

Data Availability Statement: No new data were created.

Conflicts of Interest: The authors declare no conflict of interest.

References

1. Anbar, M.; Gratt, B.M.; Hong, D. Thermology and facial telethermography. Part I: History and technical review. *Dentomaxillofacial Radiol.* **1998**, *27*, 61–67. [[CrossRef](#)] [[PubMed](#)]
2. Zhang, L.; Kumar, K.S.; He, H.; Cai, C.J.; He, X.; Gao, H.; Yue, S.; Li, C.; Seet, R.C.-S.; Ren, H. Fully organic compliant dry electrodes self-adhesive to skin for long-term motion-robust epidermal biopotential monitoring. *Nat. Commun.* **2020**, *11*, 4683. [[CrossRef](#)]
3. Narayanamurthy, V.; Padmapriya, P.; Noorasafirin, A.; Pooja, B.; Hema, K.; Nithyakalyani, K.; Samsuri, F. Skin cancer detection using non-invasive techniques. *RSC Adv.* **2018**, *8*, 28095–28130. [[CrossRef](#)] [[PubMed](#)]
4. Webb, R.C.; Bonifas, A.P.; Behnaz, A.; Zhang, Y.; Yu, K.J.; Cheng, H.; Shi, M.; Bian, Z.; Liu, Z.; Kim, Y.-S.; et al. Ultrathin conformal devices for precise and continuous thermal characterization of human skin. *Nat. Mater.* **2013**, *12*, 938. [[CrossRef](#)] [[PubMed](#)]
5. Stauffer, F.; Thielen, M.; Sauter, C.; Chardonens, S.; Bachmann, S.; Tybrandt, K.; Peters, C.; Hierold, C.; Vörös, J. Skin Conformal Polymer Electrodes for Clinical ECG and EEG Recordings. *Adv. Heal. Mater.* **2018**, *7*, e1700994. [[CrossRef](#)]
6. JLee, J.-W.; Yun, K.-S. ECG Monitoring Garment Using Conductive Carbon Paste for Reduced Motion Artifacts. *Polymers* **2017**, *9*, 439. [[CrossRef](#)]
7. Biondi, A.; Santoro, V.; Viana, P.F.; Laiou, P.; Pal, D.K.; Bruno, E.; Richardson, M.P. Noninvasive mobile EEG as a tool for seizure monitoring and management: A systematic review. *Epilepsia* **2022**, *63*, 1041–1063. [[CrossRef](#)]
8. Liu, Y.; Pharr, M.; Salvatore, G.A. Lab-on-Skin: A Review of Flexible and Stretchable Electronics for Wearable Health Monitoring. *ACS Nano* **2017**, *11*, 9614–9635. [[CrossRef](#)]
9. Tierney, M.J.; Tamada, J.A.; Potts, R.O.; Jovanovic, L.; Garg, S. Clinical evaluation of the GlucoWatch@biographer: A continual, non-invasive glucose monitor for patients with diabetes. *Biosens. Bioelectron.* **2001**, *16*, 621–629. [[CrossRef](#)]
10. Hussain, A.M.; Hussain, M.M. CMOS-Technology-Enabled Flexible and Stretchable Electronics for Internet of Everything Applications. *Adv. Mater.* **2016**, *28*, 4219–4249. [[CrossRef](#)]
11. Khan, Y.; Ostfeld, A.E.; Lochner, C.M.; Pierre, A.; Arias, A.C. Monitoring of Vital Signs with Flexible and Wearable Medical Devices. *Adv. Mater.* **2016**, *28*, 4373–4395. [[CrossRef](#)]
12. Trung, T.Q.; Lee, N.-E. Flexible and Stretchable Physical Sensor Integrated Platforms for Wearable Human-Activity Monitoring and Personal Healthcare. *Adv. Mater.* **2016**, *28*, 4338–4372. [[CrossRef](#)]
13. Honghui, J. Motion-Aircraft Resistant Design of Photoplethysmograph Ring Sensor for Driver Monitoring. Doctoral Dissertation, Massachusetts Institute of Technology, Cambridge, MA, USA, 2004.
14. Whitton, J.T.; Everall, J.D. The thickness of the epidermis. *Br. J. Dermatol.* **1973**, *89*, 467–476. [[CrossRef](#)]
15. Arumugam, V.; Naresh, M.D.; Sanjeevi, R. Effect of strain rate on the fracture behaviour of skin. *J. Biosci.* **1994**, *19*, 307–313. [[CrossRef](#)]
16. Flint, M. The biological basis of Langer’s lines. In *The Ultrastructure of Collagen*; Charles Thomas Springfield: Springfield, IL, USA, 1976; pp. 132–140.
17. Gallagher, A.J.; Annaidh, A.N.; Bruyère, K. *Dynamic Tensile Properties of Human Skin*; International Research Council on the Biomechanics of Injury: Dublin, Ireland, 2012.
18. Pawlaczyk, M.; Lełonkiewicz, M.; Wiczorowski, M. Age-dependent biomechanical properties of the skin. *Adv. Dermatol. Allergol. Postępy Dermatol. I Alergol.* **2013**, *30*, 302. [[CrossRef](#)] [[PubMed](#)]

19. Joodaki, H.; Panzer, M.B. Skin mechanical properties and modeling: A review. *Proc. Inst. Mech. Eng. Part H J. Eng. Med.* **2018**, *232*, 323–343. [[CrossRef](#)]
20. Bader, D.L.; Bowker, P. Mechanical characteristics of skin and underlying tissues in vivo. *Biomaterials* **1983**, *4*, 305–308. [[CrossRef](#)]
21. Sanders, R. Torsional elasticity of human skin in vivo. *Pflügers Arch.* **1973**, *342*, 255–260. [[CrossRef](#)]
22. Escoffier, C.; de Rigal, J.; Rochefort, A.; Vasselet, R.; Lévêque, J.-L.; Agache, P.G. Age-related mechanical properties of human skin: An in vivo study. *J. Investig. Dermatol.* **1989**, *93*, 53–357. [[CrossRef](#)]
23. Manschot, J.F.M.; Brakkee, A.J.M. The measurement and modelling of the mechanical properties of human skin in vivo—I. The measurement. *J. Biomech.* **1986**, *19*, 511–515. [[CrossRef](#)] [[PubMed](#)]
24. Grahame, R.; Holt, P.J.L. The Influence of Ageing on the in vivo Elasticity of Human Skin. *Gerontology* **1969**, *15*, 121–139. [[CrossRef](#)] [[PubMed](#)]
25. García de Arquer, F.P.; Armin, A.; Meredith, P.; Sargent, E.H. Solution-processed semiconductors for next-generation photodetectors. *Nat. Rev. Mater.* **2017**, *2*, 16100. [[CrossRef](#)]
26. Li, H.; Mao, P.; Davis, M.; Yu, Z. PEDOT:PSS-polyethylene oxide composites for stretchable and 3D-Printed thermoelectric devices. *Compos. Commun.* **2021**, *23*, 100599. [[CrossRef](#)]
27. Bielecka, U.; Lutsyk, P.; Janus, K.; Sworakowski, J.; Bartkowiak, W. Effect of solution aging on morphology and electrical characteristics of regioregular P3HT FETs fabricated by spin coating and spray coating. *Org. Electron.* **2011**, *12*, 1768–1776. [[CrossRef](#)]
28. Wu, H.; Kong, D.; Ruan, Z.; Hsu, P.-C.; Wang, S.; Yu, Z.; Carney, T.J.; Hu, L.; Fan, S.; Cui, Y. A transparent electrode based on a metal nanotrough network. *Nat. Nanotechnol.* **2013**, *8*, 421. [[CrossRef](#)]
29. Sekitani, T.; Nakajima, H.; Maeda, H.; Fukushima, T.; Aida, T.; Hata, K.; Someya, T. Stretchable active-matrix organic light-emitting diode display using printable elastic conductors. *Nat. Mater.* **2009**, *8*, 494–499. [[CrossRef](#)]
30. Kim, T.; Park, J.; Sohn, J.; Cho, D.; Jeon, S. Bioinspired, Highly Stretchable, and Conductive Dry Adhesives Based on 1D–2D Hybrid Carbon Nanocomposites for All-in-One ECG Electrodes. *ACS Nano* **2016**, *10*, 4770–4778. [[CrossRef](#)]
31. Fan, J.A.; Yeo, W.-H.; Su, Y.; Hattori, Y.; Lee, W.; Jung, S.-Y.; Zhang, Y.; Liu, Z.; Cheng, H.; Falgout, L.; et al. Fractal design concepts for stretchable electronics. *Nat. Commun.* **2014**, *5*, 3266. [[CrossRef](#)]
32. Wang, C.; Chen, X.; Wang, L.; Makihata, M.; Liu, H.-C.; Zhou, T.; Zhao, X. Bioadhesive ultrasound for long-term continuous imaging of diverse organs. *Science* **2022**, *377*, 517–523. [[CrossRef](#)]
33. Lipomi, D.J.; Tee, B.C.-K.; Vosgueritchian, M.; Bao, Z. Stretchable Organic Solar Cells. *Adv. Mater.* **2011**, *23*, 1771–1775. [[CrossRef](#)]
34. Kaltenbrunner, M.; White, M.S.; Glowacki, E.D.; Sekitani, T.; Someya, T.; Sariciftci, N.S.; Bauer, S. Ultrathin and lightweight organic solar cells with high flexibility. *Nat. Commun.* **2012**, *3*, 770. [[CrossRef](#)] [[PubMed](#)]
35. Holloway, P.H. Gold/chromium metallizations for electronic devices. *Gold Bull.* **1979**, *12*, 99–106. [[CrossRef](#)]
36. Kim, D.-H.; Lu, N.; Ma, R.; Kim, Y.-S.; Kim, R.-H.; Wang, S.; Wu, J.; Won, S.M.; Tao, H.; Islam, A.; et al. Epidermal Electronics. *Science* **2011**, *333*, 838–843. [[CrossRef](#)] [[PubMed](#)]
37. Xu, B.; Akhtar, A.; Liu, Y.; Chen, H.; Yeo, W.-H.; Park, S.I.; Boyce, B.; Kim, H.; Yu, J.; Lai, H.-Y.; et al. An Epidermal Stimulation and Sensing Platform for Sensorimotor Prosthetic Control, Management of Lower Back Exertion, and Electrical Muscle Activation. *Adv. Mater.* **2016**, *28*, 4462–4471. [[CrossRef](#)]
38. Jiang, H.; Khang, D.-Y.; Song, J.; Sun, Y.; Huang, Y.; Rogers, J.A. Finite deformation mechanics in buckled thin films on compliant supports. *Proc. Natl. Acad. Sci. USA* **2007**, *104*, 15607–15612. [[CrossRef](#)]
39. Song, J.; Jiang, H.; Liu, Z.J.; Khang, D.Y.; Huang, Y.; Rogers, J.A.; Lu, C.; Koh, C.G. Buckling of a stiff thin film on a compliant substrate in large deformation. *Int. J. Solids Struct.* **2008**, *45*, 3107–3121. [[CrossRef](#)]
40. Wolfe, S.; Cage, G.; Epstein, M.; Tice, L.; Miller, H.; Gordon, R. Metabolic studies of isolated human eccrine sweat glands. *J. Clin. Investig.* **1970**, *49*, 1880–1884. [[CrossRef](#)]
41. Martínez-Corral, I.; Olmeda, D.; Diéguez-Hurtado, R.; Tammela, T.; Alitalo, K.; Ortega, S. In vivo imaging of lymphatic vessels in development, wound healing, inflammation, and tumor metastasis. *Proc. Natl. Acad. Sci. USA* **2012**, *109*, 6223–6228. [[CrossRef](#)]
42. Lee, S.-J.; Park, C.; Lee, J.Y.; Kim, S.; Kwon, P.J.; Kim, W.; Jeon, Y.H.; Lee, E.; Yoon, Y.-S. Generation of pure lymphatic endothelial cells from human pluripotent stem cells and their therapeutic effects on wound repair. *Sci. Rep.* **2015**, *5*, 11019. [[CrossRef](#)]
43. Baura, G.D. Preface. In *Medical Device Technologies*; Baura, G.D., Ed.; Academic Press: Oxford, UK, 2012; pp. ix–xi. [[CrossRef](#)]
44. Council, N.R. *Expanding the Vision of Sensor Materials*; National Academies Press: Cambridge, MA, USA, 1995.
45. Göpel, W.; Grandke, T.; Hesse, J.; Ko, W.H.; Zemel, J.N. *Sensors: Fundamentals and General Aspects*; VCH Publishers: Weinheim, Germany, 1989; Volume 1.
46. Yamamoto, Y.; Yamamoto, D.; Takada, M.; Naito, H.; Arie, T.; Akita, S.; Takei, K. Efficient Skin Temperature Sensor and Stable Gel-Less Sticky ECG Sensor for a Wearable Flexible Healthcare Patch. *Adv. Healthc. Mater.* **2017**, *6*, 1700495. [[CrossRef](#)]
47. Bae, W.G.; Kim, D.; Kwak, M.K.; Ha, L.; Kang, S.M.; Suh, K.Y. Enhanced Skin Adhesive Patch with Modulus-Tunable Composite Micropillars. *Adv. Healthc. Mater.* **2013**, *2*, 109–113. [[CrossRef](#)] [[PubMed](#)]
48. Norton, J.J.S.; Lee, D.S.; Lee, J.W.; Lee, W.; Kwon, O.; Won, P.; Jung, S.-Y.; Cheng, H.; Jeong, J.-W.; Akce, A.; et al. Soft, curved electrode systems capable of integration on the auricle as a persistent brain–computer interface. *Proc. Natl. Acad. Sci. USA* **2015**, *112*, 3920–3925. [[CrossRef](#)]
49. Lee, S.M.; Byeon, H.J.; Lee, J.H.; Baek, D.H.; Lee, K.H.; Hong, J.S.; Lee, S.-H. Self-adhesive epidermal carbon nanotube electronics for tether-free long-term continuous recording of biosignals. *Sci. Rep.* **2014**, *4*, 6074. [[CrossRef](#)] [[PubMed](#)]

50. Tian, L.; Zimmerman, B.; Akhtar, A.; Yu, K.J.; Moore, M.; Wu, J.; Larsen, R.J.; Lee, J.W.; Li, J.; Liu, Y.; et al. Large-area MRI-compatible epidermal electronic interfaces for prosthetic control and cognitive monitoring. *Nat. Biomed. Eng.* **2019**, *3*, 194–205. [[CrossRef](#)] [[PubMed](#)]
51. Jang, K.-I.; Jung, H.N.; Lee, J.W.; Xu, S.; Liu, Y.H.; Ma, Y.; Jeong, J.-W.; Song, Y.M.; Kim, J.; Kim, B.H.; et al. Ferromagnetic, Folded Electrode Composite as a Soft Interface to the Skin for Long-Term Electrophysiological Recording. *Adv. Funct. Mater.* **2016**, *26*, 7281–7290. [[CrossRef](#)] [[PubMed](#)]
52. Hattori, Y.; Falgout, L.; Lee, W.; Jung, S.-Y.; Poon, E.; Lee, J.W.; Na, I.; Geisler, A.; Sadhwani, D.; Zhang, Y.; et al. Multifunctional Skin-Like Electronics for Quantitative, Clinical Monitoring of Cutaneous Wound Healing. *Adv. Healthc. Mater.* **2014**, *3*, 1597–1607. [[CrossRef](#)] [[PubMed](#)]
53. Madhvapathy, S.; Ma, Y.; Patel, M.; Krishnan, S.; Wei, C.; Li, Y.; Xu, S.; Feng, X.; Huang, Y.-S.; Rogers, J. Epidermal Electronic Systems for Measuring the Thermal Properties of Human Skin at Depths of up to Several Millimeters. *Adv. Funct. Mater.* **2018**, *28*, 1802083. [[CrossRef](#)]
54. Shin, J.; Jeong, B.; Kim, J.; Nam, V.B.; Yoon, Y.; Jung, J.; Hong, S.; Lee, H.; Eom, H.; Yeo, J. Sensitive wearable temperature sensor with seamless monolithic integration. *Adv. Mater.* **2020**, *32*, 1905527. [[CrossRef](#)]
55. Yu, Y.; Peng, S.; Blanloeuil, P.; Wu, S.; Wang, C.H. Wearable Temperature Sensors with Enhanced Sensitivity by Engineering Microcrack Morphology in PEDOT:PSS–PDMS Sensors. *ACS Appl. Mater. Interfaces* **2020**, *12*, 36578–36588. [[CrossRef](#)]
56. Webb, R.C.; Ma, Y.; Krishnan, S.; Li, Y.; Yoon, S.; Guo, X.; Feng, X.; Shi, Y.; Seidel, M.; Cho, N.H.; et al. Epidermal devices for noninvasive, precise, and continuous mapping of macrovascular and microvascular blood flow. *Sci. Adv.* **2015**, *1*, e1500701. [[CrossRef](#)]
57. Webb, R.C.; Pielak, R.M.; Bastien, P.; Ayers, J.; Niittynen, J.; Kurniawan, J.; Manco, M.; Lin, A.; Cho, N.H.; Malyrchuk, V.; et al. Thermal transport characteristics of human skin measured in vivo using ultrathin conformal arrays of thermal sensors and actuators. *PLoS ONE* **2015**, *10*, e0118131. [[CrossRef](#)] [[PubMed](#)]
58. Lochner, C.M.; Khan, Y.; Pierre, A.; Arias, A.C. All-organic optoelectronic sensor for pulse oximetry. *Nat. Commun.* **2014**, *5*, 5745. [[CrossRef](#)] [[PubMed](#)]
59. Yokota, T.; Zalar, P.; Kaltenbrunner, M.; Jinno, H.; Matsuhisa, N.; Kitanosako, H.; Tachibana, Y.; Yukita, W.; Koizumi, M.; Someya, T. Ultraflexible organic photonic skin. *Sci. Adv.* **2016**, *2*, e1501856. [[CrossRef](#)] [[PubMed](#)]
60. Choong, C.-L.; Shim, M.-B.; Lee, B.-S.; Jeon, S.; Ko, D.-S.; Kang, T.-H.; Bae, J.; Lee, S.H.; Byun, K.-E.; Im, J.; et al. Highly Stretchable Resistive Pressure Sensors Using a Conductive Elastomeric Composite on a Micropyramid Array. *Adv. Mater.* **2014**, *26*, 3451–3458. [[CrossRef](#)]
61. Pang, Y.; Zhang, K.; Yang, Z.; Jiang, S.; Ju, Z.; Li, Y.; Wang, X.; Wang, D.; Jian, M.; Zhang, Y.; et al. Epidermis Microstructure Inspired Graphene Pressure Sensor with Random Distributed Spinosum for High Sensitivity and Large Linearity. *ACS Nano* **2018**, *12*, 2346–2354. [[CrossRef](#)] [[PubMed](#)]
62. Guo, Y.; Guo, Z.; Zhong, M.; Wan, P.; Zhang, W.; Zhang, L. A Flexible Wearable Pressure Sensor with Bioinspired Microcrack and Interlocking for Full-Range Human–Machine Interfacing. *Small* **2018**, *14*, 1803018. [[CrossRef](#)]
63. Gao, Y.; Ota, H.; Schaler, E.W.; Chen, K.; Zhao, A.; Gao, W.; Fahad, H.M.; Leng, Y.; Zheng, A.; Xiong, F.; et al. Wearable Microfluidic Diaphragm Pressure Sensor for Health and Tactile Touch Monitoring. *Adv. Mater.* **2017**, *29*, 1701985. [[CrossRef](#)]
64. Boutry, C.M.; Nguyen, A.; Lawal, Q.O.; Chortos, A.; Rondeau-Gagné, S.; Bao, Z. A Sensitive and Biodegradable Pressure Sensor Array for Cardiovascular Monitoring. *Adv. Mater.* **2015**, *27*, 6954–6961. [[CrossRef](#)]
65. Sharma, S.; Chhetry, A.; Sharifuzzaman, M.; Yoon, H.; Park, J.Y. Wearable Capacitive Pressure Sensor Based on MXene Composite Nanofibrous Scaffolds for Reliable Human Physiological Signal Acquisition. *ACS Appl. Mater. Interfaces* **2020**, *12*, 22212–22224. [[CrossRef](#)]
66. Chen, L.Y.; Tee, B.C.K.; Chortos, A.L.; Schwartz, G.; Tse, V.J.; Lipomi, D.; Wong, H.S.P.; McConnell, M.V.; Bao, Z. Continuous wireless pressure monitoring and mapping with ultra-small passive sensors for health monitoring and critical care. *Nat. Commun.* **2014**, *5*, 5028. [[CrossRef](#)]
67. Sekine, T.; Gaitis, A.; Sato, J.; Miyazawa, K.; Muraki, K.; Shiwaku, R.; Takeda, Y.; Matsui, H.; Kumaki, D.; Domingues Dos Santos, F.; et al. Low Operating Voltage and Highly Pressure-Sensitive Printed Sensor for Healthcare Monitoring with Analogic Amplifier Circuit. *ACS Appl. Electron. Mater.* **2019**, *1*, 246–252. [[CrossRef](#)]
68. Dagdeviren, C.; Su, Y.; Joe, P.; Yona, R.; Liu, Y.; Kim, Y.-S.; Huang, Y.; Damadoran, A.R.; Xia, J.; Martin, L.W.; et al. Conformable amplified lead zirconate titanate sensors with enhanced piezoelectric response for cutaneous pressure monitoring. *Nat. Commun.* **2014**, *5*, 4496. [[CrossRef](#)]
69. Dagdeviren, C.; Shi, Y.; Joe, P.; Ghaffari, R.; Balooch, G.; Usgaonkar, K.; Gur, O.; Tran, P.L.; Crosby, J.R.; Meyer, M.; et al. Conformal piezoelectric systems for clinical and experimental characterization of soft tissue biomechanics. *Nat. Mater.* **2015**, *14*, 728. [[CrossRef](#)]
70. Su, Y.; Chen, C.; Pan, H.; Yang, Y.; Chen, G.; Zhao, X.; Li, W.; Gong, Q.; Xie, G.; Zhou, Y.; et al. Muscle Fibers Inspired High-Performance Piezoelectric Textiles for Wearable Physiological Monitoring. *Adv. Funct. Mater.* **2021**, *31*, 2010962. [[CrossRef](#)]
71. Hu, H.; Huang, H.; Li, M.; Gao, X.; Yin, L.; Qi, R.; Wu, R.S.; Chen, X.; Ma, Y.; Shi, K.; et al. A wearable cardiac ultrasound imager. *Nature* **2023**, *613*, 667–675. [[CrossRef](#)]
72. Carter, M.; Shieh, J.C. *Guide to Research Techniques in Neuroscience*; Academic Press: Cambridge, MA, USA, 2015.

73. Michael, J.; Shea, M. Electrocardiography (ECG; EKG). Available online: <https://www.merckmanuals.com/home/heart-and-blood-vessel-disorders/diagnosis-of-heart-and-blood-vessel-disorders/electrocardiography> (accessed on 1 January 2023).
74. Experiments, J.o.V. Acquisition and Analysis of an ECG (Electrocardiography) Signal. Available online: <https://www.jove.com/science-education/10473> (accessed on 1 January 2023).
75. The McGill Physiology Virtual Lab—Cardiovascular Laboratory. Available online: <https://www.medicine.mcgill.ca/physio/vlab/cardio/ECGbasics.htm> (accessed on 1 January 2023).
76. Biel, L.; Pettersson, O.; Philipson, L.; Wide, P. ECG analysis: A new approach in human identification. *IEEE Trans. Instrum. Meas.* **2001**, *50*, 808–812. [[CrossRef](#)]
77. Sharma, L.N.; Tripathy, R.K.; Dandapat, S. Multiscale Energy and Eigenspace Approach to Detection and Localization of Myocardial Infarction. *IEEE Trans. Biomed. Eng.* **2015**, *62*, 1827–1837. [[CrossRef](#)] [[PubMed](#)]
78. Luz, E.J.d.S.; Schwartz, W.R.; Cámara-Chávez, G.; Menotti, D. ECG-based heartbeat classification for arrhythmia detection: A survey. *Comput. Methods Programs Biomed.* **2016**, *127*, 144–164. [[CrossRef](#)] [[PubMed](#)]
79. Stamkopoulos, T.; Diamantaras, K.; Maglaveras, N.; Strintzis, M. ECG analysis using nonlinear PCA neural networks for ischemia detection. *IEEE Trans. Signal Process.* **1998**, *46*, 3058–3067. [[CrossRef](#)]
80. Bacharova, L.M.; Schocken, D.; H Estes, E.; Strauss, D. The role of ECG in the diagnosis of left ventricular hypertrophy. *Curr. Cardiol. Rev.* **2014**, *10*, 257–261. [[CrossRef](#)] [[PubMed](#)]
81. Bredahl, K.; Eldrup, N.; Meyer, C.; Eiberg, J.; Sillesen, H. Reproducibility of ECG-gated ultrasound diameter assessment of small abdominal aortic aneurysms. *Eur. J. Vasc. Endovasc. Surg.* **2013**, *45*, 235–240. [[CrossRef](#)] [[PubMed](#)]
82. Empson, R. FDA Approves AliveCor’s Heart Monitor for the Iphone. Available online: <https://techcrunch.com/2012/12/04/mobile-health-moves-forward-fda-approves-alivecors-heart-monitor-for-the-iphone/> (accessed on 1 January 2023).
83. Wasimuddin, M.; Elleithy, K.; Abuzneid, A.S.; Faezipour, M.; Abuzagheh, O. Stages-Based ECG Signal Analysis From Traditional Signal Processing to Machine Learning Approaches: A Survey. *IEEE Access* **2020**, *8*, 177782–177803. [[CrossRef](#)]
84. Malmivuo, J.; Plonsey, R. *Bioelectromagnetism. 13. Electroencephalography*; Oxford Univ. Press: Oxford, UK, 1995; pp. 247–264.
85. Fürbass, F. EEG Monitoring Based on Automatic Detection of Seizures and Repetitive Discharges. Doctoral Dissertation, Technische Universität Wien, Vienna, Austria, 2017.
86. Pramanik, P.K.D.; Upadhyaya, B.K.; Pal, S.; Pal, T. Chapter 1—Internet of things, smart sensors, and pervasive systems: Enabling connected and pervasive healthcare. In *Healthcare Data Analytics and Management*; Dey, N., Ashour, A.S., Bhatt, C., James Fong, S., Eds.; Academic Press: Cambridge, MA, USA, 2019; pp. 1–58. [[CrossRef](#)]
87. Gibbs, F.A.; Gibbs, E.L. *Atlas of Electroencephalography*; F. A. Gibbs, Boston City Hospital: Boston, MA, USA, 1941.
88. Kanda, P.A.d.M.; Anghinah, R.; Smidth, M.T.; Silva, J.M. The clinical use of quantitative EEG in cognitive disorders. *Dement. Neuropsychol.* **2009**, *3*, 195–203. [[CrossRef](#)] [[PubMed](#)]
89. Noachtar, S.; Rémi, J. The role of EEG in epilepsy: A critical review. *Epilepsy Behav.* **2009**, *15*, 22–33. [[CrossRef](#)]
90. Selvam, V.S.; Devi, S.S. Analysis of spectral features of EEG signal in brain tumor condition. *Meas. Sci. Rev.* **2015**, *15*, 219. [[CrossRef](#)]
91. Nuwer, M.R.; Hovda, D.A.; Schrader, L.M.; Vespa, P.M. Routine and quantitative EEG in mild traumatic brain injury. *Clin. Neurophysiol.* **2005**, *116*, 2001–2025. [[CrossRef](#)]
92. Han, C.-X.; Wang, J.; Yi, G.-S.; Che, Y.-Q. Investigation of EEG abnormalities in the early stage of Parkinson’s disease. *Cogn. Neurodyn.* **2013**, *7*, 351–359. [[CrossRef](#)]
93. Sartori, M.; Gizzi, L.; Lloyd, D.; Farina, D. A musculoskeletal model of human locomotion driven by a low dimensional set of impulsive excitation primitives. *Front. Comput. Neurosci.* **2013**, *7*, 79. [[CrossRef](#)]
94. Picard, N.; Strick, P.L. Motor Areas of the Medial Wall: A Review of Their Location and Functional Activation. *Cereb. Cortex* **1996**, *6*, 342–353. [[CrossRef](#)] [[PubMed](#)]
95. Azim, M.R.; Haque, S.A.; Amin, M.S.; Latif, T. Analysis of EEG and EMG signals for detection of Sleep Disordered Breathing events. In Proceedings of the International Conference on Electrical & Computer Engineering (ICECE 2010), Dhaka, Bangladesh, 18–20 December 2010; pp. 646–649.
96. Adel, T.; Stashuk, D. Clinical Quantitative Electromyography. In *Electrodiagnosis in New Frontiers of Clinical Research*; IntechOpen: London, UK, 22 May 2013.
97. Fuglsang-Frederiksen, A. The role of different EMG methods in evaluating myopathy. *Clin. Neurophysiol.* **2006**, *117*, 1173–1189. [[CrossRef](#)]
98. Furby, A.; Behin, A.; Lefaucheur, J.-P.; Beauvais, K.; Marcorelles, P.; Mussini, J.-M.; Bassez, G.; Créange, A.; Eymard, B.; Pénisson-Besnier, I. Late-onset cervicospinal muscle atrophy and weakness after radiotherapy for Hodgkin disease: A case series. *J. Neurol. Neurosurg. Psychiatry* **2010**, *81*, 101–104. [[CrossRef](#)] [[PubMed](#)]
99. Sakakibara, R.; Uchiyama, T.; Yamanishi, T.; Kishi, M. Sphincter EMG as a diagnostic tool in autonomic disorders. *Clin. Auton. Res.* **2009**, *19*, 20–31. [[CrossRef](#)]
100. Mills, K.R. The basics of electromyography. *J. Neurol. Neurosurg. Psychiatry* **2005**, *76*, ii32–ii35. [[CrossRef](#)] [[PubMed](#)]
101. Griffiths, I.R.; Duncan, I.D. The use of electromyography and nerve conduction studies in the evaluation of lower motor neurone disease or injury. *J. Small Anim. Pract.* **1978**, *19*, 329–340. [[CrossRef](#)] [[PubMed](#)]
102. Acharya, U.R.; Oh, S.L.; Hagiwara, Y.; Tan, J.H.; Adeli, H. Deep convolutional neural network for the automated detection and diagnosis of seizure using EEG signals. *Comput. Biol. Med.* **2018**, *100*, 270–278. [[CrossRef](#)]

103. Ferree, T.C.; Luu, P.; Russell, G.S.; Tucker, D.M. Scalp electrode impedance, infection risk, and EEG data quality. *Clin. Neurophysiol.* **2001**, *112*, 536–544. [[CrossRef](#)]
104. Zepeda-Carapia, I.; Marquez-Espinoza, A.; Alvarado-Serrano, C. Measurement of Skin-Electrode Impedance for a 12-Lead Electrocardiogram; 2005, Measurement of skin-electrode impedance for a 12-lead electrocardiogram. In Proceedings of the 2005 2nd International Conference on Electrical and Electronics Engineering, Mexico City, Mexico, 7–9 September 2005; pp. 193–195. [[CrossRef](#)]
105. Jung, H.; Moon, J.; Baek, D.; Lee, J.; Choi, Y.; Hong, J.; Lee, S. CNT/PDMS Composite Flexible Dry Electrodes for Long-Term ECG Monitoring. *IEEE Trans. Biomed. Eng.* **2012**, *59*, 1472–1479. [[CrossRef](#)]
106. Da Silva, L.F.; Dillard, D.A.; Blackman, B.; Adams, R.D. *Testing Adhesive Joints: Best Practices*; John Wiley & Sons: Hoboken, NJ, USA, 2012.
107. Izadi, H.; Penlidis, A. Polymeric Bio-Inspired Dry Adhesives: Van der Waals or Electrostatic Interactions? *Macromol. React. Eng.* **2013**, *7*, 588–608. [[CrossRef](#)]
108. Horn, R.G.; Smith, D.T. Contact Electrification and Adhesion between Dissimilar Materials. *Science* **1992**, *256*, 362–364. [[CrossRef](#)]
109. Gu, Z.; Li, S.; Zhang, F.; Wang, S. Understanding Surface Adhesion in Nature: A Peeling Model. *Adv. Sci.* **2016**, *3*, 1500327. [[CrossRef](#)]
110. Pressure Sensitive. Available online: <https://www.adhesives.org/adhesives-sealants/adhesives-sealants-overview/adhesive-technologies/pressure-sensitive> (accessed on 1 January 2023).
111. Ritter, P.; Villringer, A. Simultaneous EEG–fMRI. *Neurosci. Biobehav. Rev.* **2006**, *30*, 823–838. [[CrossRef](#)] [[PubMed](#)]
112. Maughan, R.J.; Shirreffs, S.M.; Watson, P. Exercise, Heat, Hydration and the Brain. *J. Am. Coll. Nutr.* **2007**, *26*, 604S–612S. [[CrossRef](#)] [[PubMed](#)]
113. Clark, R.P. Chapter 4 Human Skin Temperature and Convective Heat Loss. In *Studies in Environmental Science*; Cena, K., Clark, J.A., Eds.; Elsevier: Amsterdam, The Netherlands, 1981; Volume 10, pp. 57–76.
114. Ring, E.F.J.; Phillips, B. *Recent Advances in Medical Thermology*; Springer: Berlin/Heidelberg, Germany, 1984; pp. 177–183. [[CrossRef](#)]
115. Chatterjee, S.; Kyriacou, P.A. Monte Carlo Analysis of Optical Interactions in Reflectance and Transmittance Finger Photoplethysmography. *Sensors* **2019**, *19*, 789. [[CrossRef](#)]
116. Helfman, T.; Ovington, L.; Falanga, V. Occlusive dressings and wound healing. *Clin. Dermatol.* **1994**, *12*, 121–127. [[CrossRef](#)]
117. Toutouzias, K.; Benetos, G.; Drakopoulou, M.; Deligianni, C.; Spengos, K.; Stefanadis, C.; Siores, E.; Tousoulis, D. Incremental predictive value of carotid inflammation in acute ischemic stroke. *Stroke* **2015**, *46*, 272–274. [[CrossRef](#)]
118. Gautherie, M. Thermopathology of breast cancer: Measurement and analysis of in vivo temperature and blood flow. *Ann. N. Y. Acad. Sci.* **1980**, *335*, 383–415. [[CrossRef](#)]
119. Anbar, M. Clinical thermal imaging today. *IEEE Eng. Med. Biol. Mag.* **1998**, *17*, 25–33. [[CrossRef](#)]
120. Lawson, R. Implications of surface temperatures in the diagnosis of breast cancer. *Can. Med. Assoc. J.* **1956**, *75*, 309–311. [[PubMed](#)]
121. Kennedy, D.A.; Lee, T.; Seely, D. A Comparative Review of Thermography as a Breast Cancer Screening Technique. *Integr. Cancer Ther.* **2009**, *8*, 9–16. [[CrossRef](#)]
122. Kenefick, R.W.; Sollanek, K.J.; Charkoudian, N.; Sawka, M.N. Impact of skin temperature and hydration on plasma volume responses during exercise. *J. Appl. Physiol.* **2014**, *117*, 413–420. [[CrossRef](#)]
123. Sze, S.M.; Ng, K.K. *Physics of Semiconductor Devices*; John Wiley & Sons: Hoboken, NJ, USA, 2006.
124. Seebeck, T.J. *Magnetische Polarisation der Metalle und erze Durch Temperatur-Differenz*; Wilhelm Engelmann: Berlin, Germany, 1895.
125. Ioffe, A.F. *Semiconductor Thermoelements and Thermoelectric Cooling*; Infosearch Limited: London, UK, 1957.
126. Li, J.-F.; Liu, W.-S.; Zhao, L.-D.; Zhou, M. High-performance nanostructured thermoelectric materials. *NPG Asia Mater.* **2010**, *2*, 152–158. [[CrossRef](#)]
127. Dames, C. Solid-State Thermal Rectification With Existing Bulk Materials. *J. Heat Transf.* **2009**, *131*, 061301–061307. [[CrossRef](#)]
128. Grove, A.S. *Physics and Technology of Semiconductor Devices*; Wiley: Hoboken, NJ, USA, 1967.
129. Wehmeyer, G.; Yabuki, T.; Monachon, C.; Wu, J.; Dames, C. Thermal diodes, regulators, and switches: Physical mechanisms and potential applications. *Appl. Phys. Rev.* **2017**, *4*, 041304. [[CrossRef](#)]
130. Tremper, K.K. Pulse Oximetry. *CHEST* **1989**, *95*, 713–715. [[CrossRef](#)]
131. Millasseau, S.C.; Ritter, J.M.; Takazawa, K.; Chowienczyk, P.J. Contour analysis of the photoplethysmographic pulse measured at the finger. *J. Hypertens.* **2006**, *24*, 1449–1456. [[CrossRef](#)]
132. Nitzan, M.; Khanokh, B.; Slovik, Y. The difference in pulse transit time to the toe and finger measured by photoplethysmography. *Physiol. Meas.* **2001**, *23*, 85. [[CrossRef](#)]
133. Selvaraj, N.; Jaryal, A.; Santhosh, J.; Deepak, K.K.; Anand, S. Assessment of heart rate variability derived from finger-tip photoplethysmography as compared to electrocardiography. *J. Med. Eng. Technol.* **2008**, *32*, 479–484. [[CrossRef](#)]
134. Millasseau, S.; Kelly, R.; Ritter, J.; Chowienczyk, P. Determination of age-related increases in large artery stiffness by digital pulse contour analysis. *Clin. Sci.* **2002**, *103*, 371–377. [[CrossRef](#)]
135. Lax, H.; Feinberg, A.W.; Cohen, B.M. Studies of the arterial pulse wave: I. The normal pulse wave and its modification in the presence of human arteriosclerosis. *J. Chronic Dis.* **1956**, *3*, 618–631. [[CrossRef](#)]
136. Imanaga, I.; Hara, H.; Koyanagi, S.; Tanaka, K. Correlation between Wave Components of the Second Derivative of Plethysmogram and Arterial Distensibility. *Jpn. Heart J.* **1998**, *39*, 775–784. [[CrossRef](#)]

137. Takazawa, K.; Tanaka, N.; Fujita, M.; Matsuoka, O.; Saiki, T.; Aikawa, M.; Tamura, S.; Ibukiyama, C. Assessment of Vasoactive Agents and Vascular Aging by the Second Derivative of Photoplethysmogram Waveform. *Hypertension* **1998**, *32*, 365–370. [CrossRef] [PubMed]
138. Hashimoto, J.; Chonan, K.; Aoki, Y.; Nishimura, T.; Ohkubo, T.; Hozawa, A.; Suzuki, M.; Matsubara, M.; Michimata, M.; Araki, T. Pulse wave velocity and the second derivative of the finger photoplethysmogram in treated hypertensive patients: Their relationship and associating factors. *J. Hypertens.* **2002**, *20*, 2415–2422. [CrossRef]
139. Otsuka, T.; Kawada, T.; Katsumata, M.; Ibuki, C. Utility of Second Derivative of the Finger Photoplethysmogram for the Estimation of the Risk of Coronary Heart Disease in the General Population. *Circ. J.* **2006**, *70*, 304–310. [CrossRef] [PubMed]
140. Bortolotto, L.A.; Blacher, J.; Kondo, T.; Takazawa, K.; Safar, M.E. Assessment of vascular aging and atherosclerosis in hypertensive subjects: Second derivative of photoplethysmogram versus pulse wave velocity. *Am. J. Hypertens.* **2000**, *13*, 165–171. [CrossRef] [PubMed]
141. Lee, J.; Matsumura, K.; Yamakoshi, K.-i.; Rolfe, P.; Tanaka, S.; Yamakoshi, T. Comparison between red, green and blue light reflection photoplethysmography for heart rate monitoring during motion. In Proceedings of the 2013 35th Annual International Conference of the IEEE Engineering in Medicine and Biology Society (EMBC), Osaka, Japan, 3–7 July 2013; pp. 1724–1727.
142. Elsannah, F.; Bilgaiyan, A.; Affiq, M.; Shim, C.-H.; Ishidai, H.; Hattori, R. Comparative Design Study for Power Reduction in Organic Optoelectronic Pulse Meter Sensor. *Biosensors* **2019**, *9*, 48. [CrossRef] [PubMed]
143. Chung, H.; Dai, T.; Sharma, S.K.; Huang, Y.-Y.; Carroll, J.D.; Hamblin, M.R. The Nuts and Bolts of Low-level Laser (Light) Therapy. *Ann. Biomed. Eng.* **2012**, *40*, 516–533. [CrossRef]
144. Ash, C.; Dubec, M.; Donne, K.; Bashford, T. Effect of wavelength and beam width on penetration in light-tissue interaction using computational methods. *Lasers Med. Sci.* **2017**, *32*, 1909–1918. [CrossRef]
145. Minolta, K. *Basic Understanding of the Pulse Oximeter. How to Read spo2*; Konica Minolta Sensing, Inc.: Ramsey, NJ, USA, 2006.
146. Steve Underwood, V.C. A Single-Chip Pulsoximeter Design Using the MSP430. Available online: <http://www.ti.com/lit/an/slaa274b/slaa274b.pdf> (accessed on 1 January 2023).
147. Smiths Medical PM, I. How Can SpO2 Readings Differ from Manufacturer to Manufacturer? Available online: <https://www.medexsupply.com/images/How%20can%20SpO2%20readings%20differ.pdf> (accessed on 1 January 2023).
148. Design, E.C. Measuring Heart Rate and Blood Oxygen Levels for Portable Medical and Wearable Devices. Available online: <https://embeddedcomputing.com/application/healthcare/measuring-heart-rate-and-blood-oxygen-levels-for-portable-medical-and-wearable-devices> (accessed on 1 January 2023).
149. Tamura, T.; Maeda, Y.; Sekine, M.; Yoshida, M. Wearable Photoplethysmographic Sensors—Past and Present. *Electronics* **2014**, *3*, 282–302. [CrossRef]
150. Castaneda, D.; Esparza, A.; Ghamari, M.; Soltanpur, C.; Nazeran, H. A review on wearable photoplethysmography sensors and their potential future applications in health care. *Int. J. Biosens. Bioelectron.* **2018**, *4*, 195–202. [CrossRef]
151. Mendelson, Y.; Pujary, C. Measurement site and photodetector size considerations in optimizing power consumption of a wearable reflectance pulse oximeter. In Proceedings of the 25th Annual International Conference of the IEEE Engineering in Medicine and Biology Society (IEEE Cat. No.03CH37439), Cancun, Mexico, 17–21 September 2003; Volume 3014, pp. 3016–3019.
152. O'Rourke, M.F.; Hashimoto, J. Mechanical Factors in Arterial Aging. *A Clin. Perspect.* **2007**, *50*, 1–13. [CrossRef]
153. McEniery, C.M.; Cockcroft, J.R.; Roman, M.J.; Franklin, S.S.; Wilkinson, I.B. Central blood pressure: Current evidence and clinical importance. *Eur. Heart J.* **2014**, *35*, 1719–1725. [CrossRef] [PubMed]
154. Salvi, P.; Grillo, A.; Parati, G. Noninvasive estimation of central blood pressure and analysis of pulse waves by applanation tonometry. *Hypertens. Res.* **2015**, *38*, 646–648. [CrossRef] [PubMed]
155. Smulyan, H.; Siddiqui, D.S.; Carlson, R.J.; London, G.M.; Safar, M.E. Clinical Utility of Aortic Pulses and Pressures Calculated From Applanated Radial-Artery Pulses. *Hypertension* **2003**, *42*, 150–155. [CrossRef] [PubMed]
156. Takazawa, K.; Kobayashi, H.; Shindo, N.; Tanaka, N.; Yamashina, A. Relationship between Radial and Central Arterial Pulse Wave and Evaluation of Central Aortic Pressure Using the Radial Arterial Pulse Wave. *Hypertens. Res.* **2007**, *30*, 219. [CrossRef] [PubMed]
157. da Fonseca, L.J.S.; Ant, M.; Rabelo, L.A. Radial applanation tonometry as an adjuvant tool in the noninvasive arterial stiffness and blood pressure assessment. *World J. Cardiovasc. Dis.* **2014**, *2014*, 45642. [CrossRef]
158. Gratz, I.; Deal, E.; Spitz, F.; Baruch, M.; Allen, I.E.; Seaman, J.E.; Pukenas, E.; Jean, S. Continuous Non-invasive finger cuff CareTaker@comparable to invasive intra-arterial pressure in patients undergoing major intra-abdominal surgery. *BMC Anesth.* **2017**, *17*, 48. [CrossRef]
159. Huang, C.-M.; Chang, H.-C.; Kao, S.-T.; Li, T.-C.; Wei, C.-C.; Chen, C.; Liao, Y.-T.; Chen, F.-J. Radial Pressure Pulse and Heart Rate Variability in Heat- and Cold-Stressed Humans. *Evid.-Based Complement. Altern. Med.* **2011**, *2011*, 751317. [CrossRef]
160. Cattell, M.A.; Anderson, J.C.; Hasleton, P.S. Age-related changes in amounts and concentrations of collagen and elastin in normotensive human thoracic aorta. *Clin. Chim. Acta* **1996**, *245*, 73–84. [CrossRef]
161. Karamanoglu, M.; Feneley, M.P. Late systolic pressure augmentation: Role of left ventricular outflow patterns. *Am. J. Physiol.-Heart Circ. Physiol.* **1999**, *277*, H481–H487. [CrossRef]
162. Shimizu, M.; Kario, K. Review: Role of the augmentation index in hypertension. *Ther. Adv. Cardiovasc. Dis.* **2008**, *2*, 25–35. [CrossRef]

163. Mora-Urda, A.I.; Molina, M.d.C.B.; Mill, J.G.; Montero-López, P. Carotid-Femoral Pulse Wave Velocity in Healthy Spanish Children: Reference Percentile Curves. *J. Clin. Hypertens.* **2017**, *19*, 227–234. [[CrossRef](#)] [[PubMed](#)]
164. Obeid, H.; Ouedraogo, V.; Hallab, M. Arterial Stiffness: A New Biomarker to be Measured. *J. Arch. Mil. Med.* **2017**, *5*, e13204. [[CrossRef](#)]
165. Laurent, S.; Cockcroft, J.; Van Bortel, L.; Boutouyrie, P.; Giannattasio, C.; Hayoz, D.; Pannier, B.; Vlachopoulos, C.; Wilkinson, I.; Struijker-Boudier, H.; et al. Expert consensus document on arterial stiffness: Methodological issues and clinical applications. *Eur. Heart J.* **2006**, *27*, 2588–2605. [[CrossRef](#)]
166. Kim, H.-L.; Kim, S.-H. Pulse Wave Velocity in Atherosclerosis. *Front. Cardiovasc. Med.* **2019**, *6*, 41. [[CrossRef](#)] [[PubMed](#)]
167. Van Bortel, L.M.; Laurent, S.; Boutouyrie, P.; Chowienczyk, P.; Cruickshank, J.; De Backer, T.; Filipovsky, J.; Huybrechts, S.; Mattace-Raso, F.U.; Protogerou, A.D. Expert consensus document on the measurement of aortic stiffness in daily practice using carotid-femoral pulse wave velocity. *J. Hypertens.* **2012**, *30*, 445–448. [[CrossRef](#)]
168. Greenland, P.; Alpert, J.S.; Beller, G.A.; Benjamin, E.J.; Budoff, M.J.; Fayad, Z.A.; Foster, E.; Hlatky, M.A.; Hodgson, J.M.; Kushner, F.G.; et al. 2010 ACCF/AHA Guideline for Assessment of Cardiovascular Risk in Asymptomatic Adults: Executive Summary: A Report of the American College of Cardiology Foundation/American Heart Association Task Force on Practice Guidelines Developed in Collaboration With the American Society of Echocardiography, American Society of Nuclear Cardiology, Society of Atherosclerosis Imaging and Prevention, Society for Cardiovascular Angiography and Interventions, Society of Cardiovascular Computed Tomography, and Society for Cardiovascular Magnetic Resonance. *J. Am. Coll. Cardiol.* **2010**, *56*, 2182–2199. [[CrossRef](#)]
169. Rodrigues, L. The In Vivo Biomechanical Testing of the Skin and the Cosmetological Efficacy Claim Support: A Critical Overview. In *Cosmetics: Controlled Efficacy Studies and Regulation*; Elsner, P., Maibach, H.I., Merk, H.F., Eds.; Springer: Berlin/Heidelberg, Germany, 1999; pp. 197–208. [[CrossRef](#)]
170. Diridollou, S.; Black, D.; Lagarde, J.M.; Gall, Y.; Berson, M.; Vabre, V.; Patat, F.; Vaillant, L. Sex- and site-dependent variations in the thickness and mechanical properties of human skin in vivo. *Int. J. Cosmet. Sci.* **2000**, *22*, 421–435. [[CrossRef](#)]
171. Daly, C.H.; Odland, G.F. Age-related changes in the mechanical properties of human skin. *J. Investig. Dermatol.* **1979**, *73*, 84–87. [[CrossRef](#)]
172. Es' haghian, S.; Kennedy, K.M.; Gong, P.; Sampson, D.D.; McLaughlin, R.A.; Kennedy, B.F. Optical palpation in vivo: Imaging human skin lesions using mechanical contrast. *J. Biomed. Opt.* **2015**, *20*, 016013. [[CrossRef](#)]
173. Yuan, J.H.; Shi, Y.; Pharr, M.; Feng, X.; Rogers, J.A.; Huang, Y. A Mechanics Model for Sensors Imperfectly Bonded to the Skin for Determination of the Young's Moduli of Epidermis and Dermis. *J. Appl. Mech.* **2016**, *83*, 0845011–0845013. [[CrossRef](#)]
174. Wang, C.; Qi, B.; Lin, M.; Zhang, Z.; Makihata, M.; Liu, B.; Zhou, S.; Huang, Y.-h.; Hu, H.; Gu, Y.; et al. Continuous monitoring of deep-tissue haemodynamics with stretchable ultrasonic phased arrays. *Nat. Biomed. Eng.* **2021**, *5*, 749–758. [[CrossRef](#)] [[PubMed](#)]
175. Pang, C.; Lee, G.-Y.; Kim, T.-i.; Kim, S.M.; Kim, H.N.; Ahn, S.-H.; Suh, K.-Y. A flexible and highly sensitive strain-gauge sensor using reversible interlocking of nanofibres. *Nat. Mater.* **2012**, *11*, 795. [[CrossRef](#)] [[PubMed](#)]
176. Stassi, S.; Cauda, V.; Canavese, G.; Pirri, C.F. Flexible tactile sensing based on piezoresistive composites: A review. *Sensors* **2014**, *14*, 5296–5332. [[CrossRef](#)] [[PubMed](#)]
177. Li, G.; Chen, D.; Li, C.; Liu, W.; Liu, H. Engineered microstructure derived hierarchical deformation of flexible pressure sensor induces a supersensitive piezoresistive property in broad pressure range. *Adv. Sci.* **2020**, *7*, 2000154. [[CrossRef](#)]
178. Liu, Y.; Wang, H.; Zhao, W.; Qin, H.; Fang, X. Thermal-performance instability in piezoresistive sensors: Inducement and improvement. *Sensors* **2016**, *16*, 1984. [[CrossRef](#)]
179. Li, J.; Fang, L.; Sun, B.; Li, X.; Kang, S.H. Review—Recent Progress in Flexible and Stretchable Piezoresistive Sensors and Their Applications. *J. Electrochem. Soc.* **2020**, *167*, 037561. [[CrossRef](#)]
180. Shiba, K.; Imamura, G.; Yoshikawa, G. 4.3—Nanomechanical Sensors. In *Biomaterials Nanoarchitectonics*; Ebara, M., Ed.; William Andrew Publishing: Norwich, NY, USA, 2016; pp. 177–196. [[CrossRef](#)]
181. Puers, R. Capacitive sensors: When and how to use them. *Sens. Actuators A Phys.* **1993**, *37–38*, 93–105. [[CrossRef](#)]
182. Hammock, M.L.; Chortos, A.; Tee, B.C.-K.; Tok, J.B.-H.; Bao, Z. 25th Anniversary Article: The Evolution of Electronic Skin (E-Skin): A Brief History, Design Considerations, and Recent Progress. *Adv. Mater.* **2013**, *25*, 5997–6038. [[CrossRef](#)]
183. Pyo, S.; Lee, J.; Bae, K.; Sim, S.; Kim, J. Recent progress in flexible tactile sensors for human-interactive systems: From sensors to advanced applications. *Adv. Mater.* **2021**, *33*, 2005902. [[CrossRef](#)]
184. Hanna, F.F.; Yehia, A.A.; Abou-Bakr, A.F. Dielectric properties of styrene—Butadiene rubber/silicon dioxide mixtures. *Br. Polym. J.* **1973**, *5*, 83–90. [[CrossRef](#)]
185. Kim, Y.; Lee, J.; Hong, H.; Park, S.; Ryu, W. Self-Powered Wearable Micropyramid Piezoelectric Film Sensor for Real-Time Monitoring of Blood Pressure. *Adv. Eng. Mater.* **2023**, *25*, 2200873. [[CrossRef](#)]
186. Zhang, X.; Hillenbrand, J.; Sessler, G.M. Ferroelectrets with improved thermal stability made from fused fluorocarbon layers. *J. Appl. Phys.* **2007**, *101*, 054114. [[CrossRef](#)]
187. Cotton, D.P.J.; Chappell, P.H.; Cranny, A.; White, N.M.; Beeby, S.P. A Novel Thick-Film Piezoelectric Slip Sensor for a Prosthetic Hand. *IEEE Sens. J.* **2007**, *7*, 752–761. [[CrossRef](#)]
188. Xu, S.; Qin, Y.; Xu, C.; Wei, Y.; Yang, R.; Wang, Z.L. Self-powered nanowire devices. *Nat. Nanotechnol.* **2010**, *5*, 366–373. [[CrossRef](#)] [[PubMed](#)]
189. Yothers, M.P.; Browder, A.E.; Bumm, L.A. Real-space post-processing correction of thermal drift and piezoelectric actuator nonlinearities in scanning tunneling microscope images. *Rev. Sci. Instrum.* **2017**, *88*, 013708. [[CrossRef](#)] [[PubMed](#)]

190. Carovac, A.; Smajlovic, F.; Junuzovic, D. Application of ultrasound in medicine. *Acta Inf. Med.* **2011**, *19*, 168–171. [[CrossRef](#)]
191. Bhatta, A.K.; Keyal, U.; Liu, Y. Application of high frequency ultrasound in dermatology. *Discov. Med.* **2018**, *26*, 237–242.
192. Wang, C.; Li, X.; Hu, H.; Zhang, L.; Huang, Z.; Lin, M.; Zhang, Z.; Yin, Z.; Huang, B.; Gong, H.; et al. Monitoring of the central blood pressure waveform via a conformal ultrasonic device. *Nat. Biomed. Eng.* **2018**, *2*, 687–695. [[CrossRef](#)]
193. Simonsen, J.G.; Axmon, A.; Nordander, C.; Arvidsson, I. Neck and upper extremity pain in sonographers—associations with occupational factors. *Appl. Ergon.* **2017**, *58*, 245–253. [[CrossRef](#)]
194. Heres, H.M.; Sjoerdsma, M.; Schoots, T.; Rutten, M.C.; van de Vosse, F.N.; Lopata, R.G. Image acquisition stability of fixated musculoskeletal sonography in an exercise setting: A quantitative analysis and comparison with freehand acquisition. *J. Med. Ultrason.* **2020**, *47*, 47–56. [[CrossRef](#)]
195. Craig, S.S.; Craig, S.A.; Ganio, M.S.; Maresh, C.M.; Horrace, G.; da Costa, K.-A.; Zeisel, S.H. The betaine content of sweat from adolescent females. *J. Int. Soc. Sport. Nutr.* **2010**, *7*, 3. [[CrossRef](#)] [[PubMed](#)]
196. Heikenfeld, J. Technological leap for sweat sensing. *Nature* **2016**, *529*, 475. [[CrossRef](#)] [[PubMed](#)]
197. Robertson, W.G.; Marshall, R.W.; Bowers, G.N. Ionized Calcium in Body Fluids. *CRC Crit. Rev. Clin. Lab. Sci.* **1981**, *15*, 85–125. [[CrossRef](#)]
198. Patterson, M.J.; Galloway, S.D.R.; Nimmo, M.A. Variations in regional sweat composition in normal human males. *Exp. Physiol.* **2001**, *85*, 869–875. [[CrossRef](#)]
199. Sonner, Z.; Wilder, E.; Heikenfeld, J.; Kasting, G.; Beyette, F.; Swaile, D.; Sherman, F.; Joyce, J.; Hagen, J.; Kelley-Loughnane, N.; et al. The microfluidics of the eccrine sweat gland, including biomarker partitioning, transport, and biosensing implications. *Biomicrofluidics* **2015**, *9*, 031301. [[CrossRef](#)]
200. Emaminejad, S.; Gao, W.; Wu, E.; Davies, Z.A.; Yin Yin Nyein, H.; Challa, S.; Ryan, S.P.; Fahad, H.M.; Chen, K.; Shahpar, Z.; et al. Autonomous sweat extraction and analysis applied to cystic fibrosis and glucose monitoring using a fully integrated wearable platform. *Proc. Natl. Acad. Sci. USA* **2017**, *114*, 4625–4630. [[CrossRef](#)] [[PubMed](#)]
201. Gonzalo-Ruiz, J.; Mas, R.; de Haro, C.; Cabruja, E.; Camero, R.; Alonso-Lomillo, M.A.; Muñoz, F.J. Early determination of cystic fibrosis by electrochemical chloride quantification in sweat. *Biosens. Bioelectron.* **2009**, *24*, 1788–1791. [[CrossRef](#)]
202. Davis, P.B.; Drumm, M.; Konstan, M.W. Cystic fibrosis. *Am. J. Respir. Crit. Care Med.* **1996**, *154*, 1229–1256. [[CrossRef](#)]
203. Malhotra, M.S.; Sridharan, K.; Venkataswamy, Y. Potassium losses in sweat under heat stress. *Aviat Space Env. Med.* **1976**, *47*, 503–504.
204. Consolazio, C.F.; Matoush, L.O.; Nelson, R.A.; Hackler, L.R.; Preston, E.E. Relationship Between Calcium in Sweat, Calcium Balance, and Calcium Requirements. *J. Nutr.* **1962**, *78*, 78–88. [[CrossRef](#)]
205. Kehayoglou, A.K.; Holdsworth, C.D.; Agnew, J.E.; Whelton, M.J.; Sherlock, S. Bone Disease and Calcium Absorption IN Primary Biliary Cirrhosis: With Special Reference to Vitamin-D Therapy. *Lancet* **1968**, *291*, 715–719. [[CrossRef](#)]
206. Bouillon, R.; Auwerx, J.; Dekeyser, L.; Fevery, J.; Lissens, W.; De Moor, P. Serum Vitamin D Metabolites and Their Binding Protein in Patients with Liver Cirrhosis. *J. Clin. Endocrinol. Metab.* **1984**, *59*, 86–89. [[CrossRef](#)] [[PubMed](#)]
207. Gogusev, J.; Duchambon, P.; Hory, B.; Giovannini, M.; Goureau, Y.; Sarfati, E.; Drüeke, T.B. Depressed expression of calcium receptor in parathyroid gland tissue of patients with hyperparathyroidism. *Kidney Int.* **1997**, *51*, 328–336. [[CrossRef](#)] [[PubMed](#)]
208. Shawcross, D.L.; Shabbir, S.S.; Taylor, N.J.; Hughes, R.D. Ammonia and the neutrophil in the pathogenesis of hepatic encephalopathy in cirrhosis. *Hepatology* **2010**, *51*, 1062–1069. [[CrossRef](#)]
209. Bariya, M.; Yin Yin Nyein, H.; Javey, A. Wearable sweat sensors. *Nat. Electron.* **2018**, *1*, 160–171. [[CrossRef](#)]
210. Schmid-Wendtner, M.H.; Korting, H.C. The pH of the Skin Surface and Its Impact on the Barrier Function. *Ski. Pharmacol. Physiol.* **2006**, *19*, 296–302. [[CrossRef](#)]
211. Polliack, A.; Taylor, R.; Bader, D. Sweat analysis following pressure ischaemia in a group of debilitated subjects. *J. Rehabil. Res. Dev.* **1997**, *34*, 303–308. [[PubMed](#)]
212. Green, J.M.; Bishop, P.A.; Muir, I.H.; McLester Jr, J.R.; Heath, H.E. Effects of High and Low Blood Lactate Concentrations on Sweat Lactate Response. *Int. J. Sport. Med.* **2000**, *21*, 556–560. [[CrossRef](#)]
213. Correlation Between Sweat Glucose and Blood Glucose in Subjects with Diabetes. *Diabetes Technol. Ther.* **2012**, *14*, 398–402. [[CrossRef](#)]
214. Fraga, C.G. Relevance, essentiality and toxicity of trace elements in human health. *Mol. Asp. Med.* **2005**, *26*, 235–244. [[CrossRef](#)]
215. Schaefer, M.; Schellenberg, M.; Merle, U.; Weiss, K.H.; Stremmel, W. Wilson protein expression, copper excretion and sweat production in sweat glands of Wilson disease patients and controls. *BMC Gastroenterol.* **2008**, *8*, 29. [[CrossRef](#)] [[PubMed](#)]
216. Sears, M.E.; Kerr, K.J.; Bray, R.I. Arsenic, Cadmium, Lead, and Mercury in Sweat: A Systematic Review. *J. Environ. Public Health* **2012**, *2012*, 10. [[CrossRef](#)]
217. Mudgal, V.; Madaan, N.; Mudgal, A.; Singh, R.; Mishra, S. Effect of toxic metals on human health. *Open Nutraceuticals J.* **2010**, *3*, 94–99. [[CrossRef](#)]
218. Bandodkar, A.J.; Molinnus, D.; Mirza, O.; Guinovart, T.; Windmiller, J.R.; Valdés-Ramírez, G.; Andrade, F.J.; Schöning, M.J.; Wang, J. Epidermal tattoo potentiometric sodium sensors with wireless signal transduction for continuous non-invasive sweat monitoring. *Biosens. Bioelectron.* **2014**, *54*, 603–609. [[CrossRef](#)]
219. Rose, D.P.; Ratterman, M.E.; Griffin, D.K.; Hou, L.; Kelley-Loughnane, N.; Naik, R.R.; Hagen, J.A.; Papautsky, I.; Heikenfeld, J.C. Adhesive RFID Sensor Patch for Monitoring of Sweat Electrolytes. *IEEE Trans. Biomed. Eng.* **2015**, *62*, 1457–1465. [[CrossRef](#)]

220. Anastasova, S.; Crewther, B.; Bemnowicz, P.; Curto, V.; Ip, H.M.D.; Rosa, B.; Yang, G.-Z. A wearable multisensing patch for continuous sweat monitoring. *Biosens. Bioelectron.* **2017**, *93*, 139–145. [[CrossRef](#)] [[PubMed](#)]
221. Gao, W.; Emaminejad, S.; Nyein, H.Y.Y.; Challa, S.; Chen, K.; Peck, A.; Fahad, H.M.; Ota, H.; Shiraki, H.; Kiriya, D.; et al. Fully integrated wearable sensor arrays for multiplexed in situ perspiration analysis. *Nature* **2016**, *529*, 509. [[CrossRef](#)] [[PubMed](#)]
222. Nyein, H.Y.Y.; Gao, W.; Shahpar, Z.; Emaminejad, S.; Challa, S.; Chen, K.; Fahad, H.M.; Tai, L.-C.; Ota, H.; Davis, R.W.; et al. A Wearable Electrochemical Platform for Noninvasive Simultaneous Monitoring of Ca²⁺ and pH. *ACS Nano* **2016**, *10*, 7216–7224. [[CrossRef](#)]
223. Guinovart, T.; Bandodkar, A.J.; Windmiller, J.R.; Andrade, F.J.; Wang, J. A potentiometric tattoo sensor for monitoring ammonium in sweat. *Analyst* **2013**, *138*, 7031–7038. [[CrossRef](#)]
224. Gao, W.; Nyein, H.Y.Y.; Shahpar, Z.; Fahad, H.M.; Chen, K.; Emaminejad, S.; Gao, Y.; Tai, L.-C.; Ota, H.; Wu, E.; et al. Wearable Microsensor Array for Multiplexed Heavy Metal Monitoring of Body Fluids. *ACS Sens.* **2016**, *1*, 866–874. [[CrossRef](#)]
225. Kim, J.; de Araujo, W.R.; Samek, I.A.; Bandodkar, A.J.; Jia, W.; Brunetti, B.; Paixão, T.R.L.C.; Wang, J. Wearable temporary tattoo sensor for real-time trace metal monitoring in human sweat. *Electrochem. Commun.* **2015**, *51*, 41–45. [[CrossRef](#)]
226. Bandodkar, A.J.; Hung, V.W.S.; Jia, W.; Valdés-Ramírez, G.; Windmiller, J.R.; Martínez, A.G.; Ramírez, J.; Chan, G.; Kerman, K.; Wang, J. Tattoo-based potentiometric ion-selective sensors for epidermal pH monitoring. *Analyst* **2013**, *138*, 123–128. [[CrossRef](#)] [[PubMed](#)]
227. Curto, V.F.; Fay, C.; Coyle, S.; Byrne, R.; O’Toole, C.; Barry, C.; Hughes, S.; Moyna, N.; Diamond, D.; Benito-Lopez, F. Real-time sweat pH monitoring based on a wearable chemical barcode micro-fluidic platform incorporating ionic liquids. *Sens. Actuators B Chem.* **2012**, *171–172*, 1327–1334. [[CrossRef](#)]
228. Koh, A.; Kang, D.; Xue, Y.; Lee, S.; Pielak, R.M.; Kim, J.; Hwang, T.; Min, S.; Banks, A.; Bastien, P.; et al. A soft, wearable microfluidic device for the capture, storage, and colorimetric sensing of sweat. *Sci. Transl. Med.* **2016**, *8*, ra165–ra366. [[CrossRef](#)] [[PubMed](#)]
229. Gao, L.; Zhang, Y.; Malyarchuk, V.; Jia, L.; Jang, K.-I.; Chad Webb, R.; Fu, H.; Shi, Y.; Zhou, G.; Shi, L.; et al. Epidermal photonic devices for quantitative imaging of temperature and thermal transport characteristics of the skin. *Nat. Commun.* **2014**, *5*, 4938. [[CrossRef](#)]
230. Jia, W.; Bandodkar, A.J.; Valdés-Ramírez, G.; Windmiller, J.R.; Yang, Z.; Ramírez, J.; Chan, G.; Wang, J. Electrochemical Tattoo Biosensors for Real-Time Noninvasive Lactate Monitoring in Human Perspiration. *Anal. Chem.* **2013**, *85*, 6553–6560. [[CrossRef](#)]
231. Khodagholy, D.; Curto, V.F.; Fraser, K.J.; Gurfinkel, M.; Byrne, R.; Diamond, D.; Malliaras, G.G.; Benito-Lopez, F.; Owens, R.M. Organic electrochemical transistor incorporating an ionogel as a solid state electrolyte for lactate sensing. *J. Mater. Chem.* **2012**, *22*, 4440–4443. [[CrossRef](#)]
232. Song, K.; Ha, U.; Lee, J.; Bong, K.; Yoo, H. An 87-mA-min Iontophoresis Controller IC With Dual-Mode Impedance Sensor for Patch-Type Transdermal Drug Delivery System. *IEEE J. Solid-State Circuits* **2014**, *49*, 167–178. [[CrossRef](#)]
233. Zhang, L.; Lerner, S.; Rustrum, W.V.; Hofmann, G.A. Electroporation-mediated topical delivery of vitamin C for cosmetic applications. *Bioelectrochem. Bioenerg.* **1999**, *48*, 453–461. [[CrossRef](#)]
234. Kassan, D.G.; Lynch, A.M.; Stiller, M.J. Physical enhancement of dermatologic drug delivery: Iontophoresis and phonophoresis. *J. Am. Acad. Dermatol.* **1996**, *34*, 657–666. [[CrossRef](#)]
235. Magistro, C.M. A Preliminary Clinical Report: Hyaluronidase by Iontophoresis: In the Treatment of Edema. *Phys. Therapy* **1964**, *44*, 169–175. [[CrossRef](#)] [[PubMed](#)]
236. Gunawardena, H.; Harris, N.; Carmichael, C.; McHugh, N.J. Microvascular responses following digital thermal hyperaemia and iontophoresis measured by laser Doppler imaging in idiopathic inflammatory myopathy. *Rheumatology* **2007**, *46*, 1483–1486. [[CrossRef](#)] [[PubMed](#)]
237. Allwell-Brown, E.; Afuwape, O.; Ayandipo, O.; Alonge, T. Correlation of the association of serum lactate, random blood sugar, and revised trauma score as predictors of outcome in hemodynamically unstable abdominal emergencies. *Niger. J. Clin. Pract.* **2016**, *19*, 196–200.
238. Mitra, A.; Choi, S.; Boshier, P.R.; Razumovskaya-Hough, A.; Belluomo, I.; Spänel, P.; Hanna, G.B. The Human Skin Volatilome: A Systematic Review of Untargeted Mass Spectrometry Analysis. *Metabolites* **2022**, *12*, 824. [[CrossRef](#)]
239. Drabińska, N.; Flynn, C.; Ratcliffe, N.; Belluomo, I.; Myridakis, A.; Gould, O.; Fois, M.; Smart, A.; Devine, T.; Costello, B.D.L. A literature survey of all volatiles from healthy human breath and bodily fluids: The human volatilome. *J. Breath Res.* **2021**, *15*, 034001. [[CrossRef](#)]
240. Broza, Y.Y.; Zuri, L.; Haick, H. Combined Volatolomics for Monitoring of Human Body Chemistry. *Sci. Rep.* **2014**, *4*, 4611. [[CrossRef](#)] [[PubMed](#)]
241. Einoch Amor, R.; Nakhleh, M.K.; Barash, O.; Haick, H. Breath analysis of cancer in the present and the future. *European Respir. Rev.* **2019**, *28*, 190002. [[CrossRef](#)]
242. Wang, J.; Li, S.; Yi, F.; Zi, Y.; Lin, J.; Wang, X.; Xu, Y.; Wang, Z.L. Sustainably powering wearable electronics solely by biomechanical energy. *Nat. Commun.* **2016**, *7*, 12744. [[CrossRef](#)]
243. Jia, W.; Valdés-Ramírez, G.; Bandodkar, A.J.; Windmiller, J.R.; Wang, J. Epidermal Biofuel Cells: Energy Harvesting from Human Perspiration. *Angew. Chem. Int. Ed.* **2013**, *52*, 7233–7236. [[CrossRef](#)]
244. Jia, W.; Wang, X.; Imani, S.; Bandodkar, A.J.; Ramírez, J.; Mercier, P.P.; Wang, J. Wearable textile biofuel cells for powering electronics. *J. Mater. Chem. A* **2014**, *2*, 18184–18189. [[CrossRef](#)]

245. Bandodkar, A.J.; You, J.-M.; Kim, N.-H.; Gu, Y.; Kumar, R.; Mohan, A.V.; Kurniawan, J.; Imani, S.; Nakagawa, T.; Parish, B. Soft, stretchable, high power density electronic skin-based biofuel cells for scavenging energy from human sweat. *Energy Environ. Sci.* **2017**, *10*, 1581–1589. [[CrossRef](#)]
246. Berchmans, S.; Bandodkar, A.J.; Jia, W.; Ramírez, J.; Meng, Y.S.; Wang, J. An epidermal alkaline rechargeable Ag–Zn printable tattoo battery for wearable electronics. *J. Mater. Chem. A* **2014**, *2*, 15788–15795. [[CrossRef](#)]
247. El-Kady, M.F.; Strong, V.; Dubin, S.; Kaner, R.B. Laser Scribing of High-Performance and Flexible Graphene-Based Electrochemical Capacitors. *Science* **2012**, *335*, 1326–1330. [[CrossRef](#)] [[PubMed](#)]
248. Zhai, X.; Jelfs, B.; Chan, R.H.M.; Tin, C. Self-Recalibrating Surface EMG Pattern Recognition for Neuroprosthesis Control Based on Convolutional Neural Network. *Front. Neurosci.* **2017**, *11*, 379. [[CrossRef](#)] [[PubMed](#)]
249. Special Considerations: Biocompatibility. Available online: <https://www.fda.gov/medical-devices/premarket-notification-510k/special-considerations#bio> (accessed on 21 December 2018).
250. Use of International Standard ISO 10993-1, Biological Evaluation of Medical Devices—Part 1: Evaluation and Testing within a Risk Management Process. Available online: <https://www.fda.gov/media/85865/download> (accessed on 1 January 2023).
251. ISO 10993-1:2009. Biological Evaluation of Medical Devices—Part 1: Evaluation and Testing within a Risk Management Process (15 October 2009). Available online: <http://nhiso.com/wp-content/uploads/2018/05/ISO-10993-1-2009.pdf> (accessed on 1 January 2023).

Disclaimer/Publisher’s Note: The statements, opinions and data contained in all publications are solely those of the individual author(s) and contributor(s) and not of MDPI and/or the editor(s). MDPI and/or the editor(s) disclaim responsibility for any injury to people or property resulting from any ideas, methods, instructions or products referred to in the content.